

Article

Multi-Scale Modelling of the Bound Metal Deposition Manufacturing of Ti6Al4V

Dmitry G. Luchinsky ^{1,2,*}, Vasyl Hafiychuk ², Kevin R. Wheeler ³, Sudipta Biswas ⁴, Christopher E. Roberts ⁵, Ian M. Hanson ⁵, Tracie J. Prater ⁵ and Peter V. E. McClintock ¹

¹ Department of Physics, Lancaster University, Lancaster LA1 4YB, UK; p.v.e.mcclintock@lancaster.ac.uk

² KBR, Inc., Ames Research Center, Moffett Field, CA 94035, USA; vasyh.hafiychuk@nasa.gov

³ Ames Research Center, Moffett Field, CA 94035, USA; kevin.r.wheeler@nasa.gov

⁴ Computational Mechanics and Materials, Idaho National Laboratory, Idaho Falls, ID 83415, USA; sudipta.biswas@inl.gov

⁵ Marshall Space Flight Center, Huntsville, AL 35812, USA; christopher.e.roberts@nasa.gov (C.E.R.); ian.m.hanson@nasa.gov (I.M.H.); tracie.j.prater@nasa.gov (T.J.P.)

* Correspondence: dmitry.g.luchinsky@nasa.gov

Abstract: Nonlinear shrinkage of the metal part during manufacturing by bound metal deposition, both on the ground and under microgravity, is considered. A multi-scale physics-based approach is developed to address the problem. It spans timescales from atomistic dynamics on the order of nanoseconds to full-part shrinkage on the order of hours. This approach enables estimation of the key parameters of the problem, including the widths of grain boundaries, the coefficient of surface diffusion, the initial redistribution of particles during the debinding stage, the evolution of the microstructure from round particles to densely-packed grains, the corresponding changes in the total and chemical free energies, and the sintering stress. The method has been used to predict shrinkage at the levels of two particles, of the filament cross-section, of the sub-model, and of the whole green, brown, and metal parts.

Keywords: bound metal deposition; molecular dynamics; phase field approach; discrete element method; finite element method; experimental correlations



Citation: Luchinsky, D.G.; Hafiychuk, V.; Wheeler, K.R.; Biswas, S.; Roberts, C.E.; Hanson, I.M.; Prater, T.J.; McClintock, P.V.E. Multi-Scale Modelling of the Bound Metal Deposition Manufacturing of Ti6Al4V. *Thermo* **2022**, *2*, 116–148. <https://doi.org/10.3390/thermo2030011>

Academic Editor: Johan Jacquemin

Received: 27 April 2022

Accepted: 6 June 2022

Published: 23 June 2022

Publisher's Note: MDPI stays neutral with regard to jurisdictional claims in published maps and institutional affiliations.



Copyright: © 2022 by the authors. Licensee MDPI, Basel, Switzerland. This article is an open access article distributed under the terms and conditions of the Creative Commons Attribution (CC BY) license (<https://creativecommons.org/licenses/by/4.0/>).

1. Introduction

Yesterday's vision of in-space manufacturing will become tomorrow's reality [1]. This statement, made in 1993, finds its confirmation today when NASA seeks a paradigm shift in the design and manufacturing of space architectures to enable the on-demand fabrication of critical systems. In particular, the In-Space Manufacturing (ISM) project at NASA's Marshall Space Flight Center, in collaboration with industrial partners, is developing capabilities for the 3D additive manufacturing (AM) of metals in space. Research aimed at supporting 3D printing capabilities in space was reported earlier [2,3].

Here the technology of bound metal deposition (BMD) is analysed. BMD is currently being matured for International Space Station experiments. It is an extrusion-based process of additive manufacturing, sometimes referred to as shaping, debinding, sintering (SDS) [4]. In this process, metal powder—particles of micron size—are mixed with a soft binder that keeps the mixture together. During the shaping stage the mixture is usually heated to soften the binder and then dispensed through a nozzle. The exact toolpaths and extrusion rates are calculated to shape the required geometry of the part, which is called “green” at this stage.

The shaping step is followed by placing the part in the debinder and removing the binder from it. Up to 70% of the primary binder can be sometimes removed by chemical dissolution or thermal debinding, while the remaining binder helps the part to retain

its shape. The main point of interest here lies in the debinding achieved by thermal decomposition, after which the part is called “brown”.

Finally, densified metallic components are obtained through sintering. Densification occurs in two steps. First, there is necking of the powder particles [5–7]. At the next stage, sintering occurs via diffusion of vacancies along grain boundaries and free surfaces from the interior to the external surface of the sample [8–10]. Final densities can reach up to 96–99.8% of theoretical values, depending on the processing characteristics, while the part will shrink by up to 13–25%. The challenges of the latter process include possible defects in the microstructure, reduced density, residual stress, cracking, and nonlinear shrinkage of the final parts. For example, experimentally observed [11] shrinkage in the vertical direction can be as high as 25%, exceeding that in the horizontal plane by 10%. Several factors affect BMD including the particle size distribution, the packing and filling densities, the geometry of the part, gravity, the debinding process, pressure, and the temperature protocol, to mention a few.

The mechanical properties of the final part are related to the physical properties of the individual metal particles, the bulk properties of the paste, and the processing characteristics. The complexities of these multifaceted relationships [12] and of the underlying physics render modelling BMD a challenging multi-scale problem. It involves atomic diffusion at the particle–particle interface on the nanoscale [6,13,14], microstructure evolution on the microscale [14–16], initial shrinkage and densification of small printed parts with particle resolution on the mesoscale [17–20], and macroscopic modelling of the sintering of the whole part [21–23].

The difficulties are exacerbated by the fact that the analysis of each physical scale requires a different approach. Thus atomic diffusion is analysed using molecular dynamics (MD) [13] applied to a few particles. Simulations of the evolution of the microstructure are performed using phase-field methods [14–16] for tens of particles. Mesoscale dynamics is simulated by applying the discrete element modelling approach [17–20] to the tens of thousands of particles shaping a small submodel of the whole part, while macroscopic analysis is performed using the finite element method [21–23] applied to a continuous model of the whole part.

The importance of a multiscale approach to the modelling of sintering was well recognised in both earlier experimental [24] and numerical [19,25,26] research. However, the number of publications remains limited. Here this approach is extended to encompass five different methods of analysis spanning from atomic simulations to the full-scale finite element modelling of sintering of the whole part. The results of simulations on the ground will be compared with those under microgravity, for some of these methods.

In zero gravity, the problem becomes even more involved because gravity is one of the main sources of the nonlinear shrinkage [11,27,28] that results in shape distortion during sintering on the ground. “The first time someone tries to do sintering in a different gravitational environment beyond Earth, or even microgravity, they may be in for a surprise. There just aren’t enough trials yet to tell us what the outcome could be. Ultimately we have to be empirical, give it a try, and see what happens.” [29].

To extend the analysis of sintering through all of the important scales, and to understand better the corresponding interdependences, a multi-scale modelling approach has been developed spanning from the atomic scale to the dimensions of the whole part. The numerical methods in this approach include: (i) molecular dynamics using LAMMPS [30,31]; (ii) phase-field methods using Multiphysics Object-Oriented Simulation Environment—MOOSE Multiphysics [32]; (iii) discrete element modelling using KRATOS Multiphysics [33,34]; (iv) analysis of experimental correlations; (v) finite element modelling using COMSOL [35].

All these methods have their own advantages and disadvantages and, in what follows, they will be used to estimate the key parameters of the sintering dynamics on different scales. Importantly, the methods are interconnected, so that parameters estimated on one scale are used as input parameters for the next scale up. The performance of these methods

will be estimated, and a multi-scale approach combining their individual strengths will be developed.

The manuscript is organised as follows. Molecular dynamics simulations on the scale of tens of nanometers and a few nanoseconds are discussed in Section 2. Results of the phase-field modelling of the microstructure evolution in the filament cross-section are considered in Section 3. The application of discrete element modelling for analysis of the initial shrinkage and particle re-arrangement on the scale of a few millimetres and several minutes is discussed in Section 4. Analysis of experimental correlations and a simplified model of shrinkage are discussed in Section 5. Finite element modelling of shrinkage in the green, brown and metal parts is analysed in detail in Section 6. The results are summarised and discussed, and directions for future work are considered, in Section 7. Finally, conclusions are drawn in Section 8.

2. Atomistic Modelling of Sintering Ti-6Al-4V Particles

The smallest scale that allows one to simulate the coalescence of metal particles is that of atoms [19,25], ranging from single atoms up to ~ 100 nm. This allows one to simulate the sintering of a few particles on a time scale ~ 100 ns, study the sintering mechanisms, and estimate important system parameters. At the initial stage of sintering, neck growth can invoke several different diffusion mechanisms [36] including (i) surface diffusion; (ii) lattice diffusion; (iii) evaporation and condensation from the particle surface; (iv) grain boundary diffusion; (v) lattice diffusion from the grain boundary; (vi) plastic flow.

Of these mechanisms, the dominant two are (i) diffusion at the grain boundary; (ii) diffusion at the surface. The driving force for both is the gradient of the chemical potential [37,38]: (i) at the grain boundary $\mu = \mu_0 - \sigma_n \Omega$; (ii) at the surface $\mu = \mu_0 - \gamma_s \kappa \Omega$. Here μ_0 is the standard chemical potential of the material, σ_n is the normal stress at the boundary, γ_s is the surface energy, $\kappa = -2/r$ where r is the radius of the sphere is the surface curvature, and Ω is the atomic volume. The positive normal stress on the surface $\gamma_s \kappa$ is tension or, if negative, compression.

To simulate the sintering of Ti6Al4V nanoparticles, they are first built using the package AtomsK [39]. An example of the initial configuration of three particles is shown in Figure 1. The particle diameters are 14 nm for the first particle, 12 nm for the second particle, and 16 nm for the third one. The initial distance between the left and middle particles is ~ 14.25 nm and ~ 14.65 nm between the middle and right particles. Next, the input files for the LAMMPS package are generated by using AtomsK and then parameters of the modified embedded atom method (MEAM) potentials [40,41] are added to these files:

$$E = \sum_i \left(E_i(\bar{\rho}_i + \frac{1}{2} \sum_{j \neq i} \phi_{ij}(R_{ij})) \right), \quad F(\bar{\rho}) = AE_c(\bar{\rho}/\bar{\rho}^0) \ln(\bar{\rho}/\bar{\rho}^0),$$

$$\bar{\rho}_i = \bar{\rho}_i^{(0)} G(\Gamma), \quad G(\Gamma) = 2/(1 + e^{-\Gamma}), \quad \Gamma = \sum_{h=0}^3 t_i^{(h)} \left[\rho_i^{(h)} / t_i^{(0)} \right]^2.$$

$$\rho_i^{a(h)}(R) = e^{-\beta^{(h)}(R/r_e - 1)}.$$

where F is the embedding energy, which is a function of the atomic electron density ρ_i at the position of atom i , ϕ_{ij} and is a pair potential interaction, where the parameters $t_i^{(h)}$ are weight factors and the quantities $\rho_i^{(h)}$ with $h = 0, \dots, 3$, are partial electron densities, E_c cohesive energy, $\bar{\rho}^0$ is the background electron density for the reference structure, A is an adjustable parameter, R_{ij} is the distance to the j -th atom from the site i , $\beta^{(h)}$, the decay lengths are adjustable parameters, and r_e is the nearest-neighbour distance in the equilibrium reference structure. Specific parameters of the MEAM potential used in this work are listed in the Table 1, see also [42].

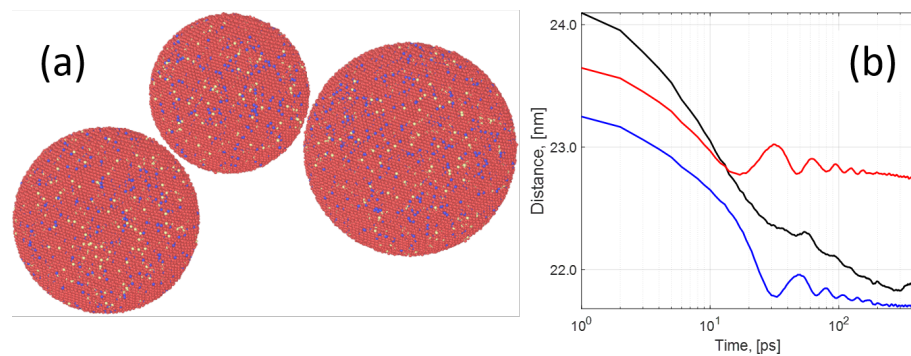


Figure 1. (a) Image (obtained with OVITO [43]) of the initial state of sintering of 3 particles with HCP crystal structure (α phase). Diameters of the particles 1 to 3 (from left to right): 1st 14 nm, 2nd 12 nm, and 3rd 16 nm. The colours show Ti (red), Al (yellow), and V (blue). (b) Distances between particles 1–2 (blue), 2–3 (red) and 1–3 (black) as a function of time during first 0.39 ns of sintering. Distance between pairs 1–2 and 2–3 is increased by 9 nm to be in scale with the distance for the pair 1–3.

Table 1. Parameters of the MEAM force field used in MD simulations.

# elt # alpha # t0	lat b0 t1	z b1 t2	ielement b2 t3	atwt b3 rozero	alat ibar	esub	asub
Al 4.975 1	fcc 3.2 3.05	12 2.6 0.51	13 6 7.75	26.9815 2.6 1	4.05 0	3.36	1.16
V 4.89 1	bcc 4.74 1.7	8 1 2.8	23 2.5 −1.6	50.942 1 1	3.04 0	5.3	1
Ti 5.03 1	hcp 2.7 6.8	12 1 −2	22 3 −12	47.867 1 1	2.95 0	4.87	0.66

The result of sintering of the three particles in the hcp crystal structure at a temperature $T = 1200$ K are shown in Figure 1b. The initial stage of sintering during the first two picoseconds can be clearly identified in the figure. Particles that are initially separated by a distance of the order 1 nm (edge-to-edge shortest distance) are mutually attracted by the van der Waals force [44]. Since their initial velocity is zero, the results allow one to estimate the magnitude of the Van der Waals forces. MD simulations also allow one to estimate the number of other important parameters required as inputs to the microscale simulations including diffusion rates and grain boundary width as will now be discussed in more detail.

Analysis of Diffusion

This section describes the analysis of the diffusion of atoms at the interface between two particles with bcc crystal structures, a diameter of 24 nm and a temperature of 1300 K. The results of the simulations are shown in Figure 2. In the top panel the atoms of the two different particles are shown in blue and pink colours, respectively, and the interface is shown by the vertical dashed line. The distribution of the titanium atoms at the boundary layer after 1 ns of simulation time is shown in Figure 2 (bottom panel). Following the distribution of atoms in time, one can estimate the distance D between the particles, the effective width of the boundary layer δ_b , and the radius of the neck R . The dependences of these parameters on time are shown in the Figure 2c,d. For example, the distance $D(t)$ between the centres of the particles is shown in the top-right inset of Figure 2c. It can be seen that the initial fast coalescence of the particles is followed by a steady decrease in $D(t)$ at a rate ≈ 0.2 nm per ns. This sintering rate corresponds to the growth of the boundary

width (≈ 0.8 nm per ns) and the neck radius (≈ 0.2 nm per ns). Note that the effective width of the boundary layer defined here is the width of the layer where atoms of both particles are mixed together. It corresponds to the width of the interface layer between the particles that cannot be uniquely attributed to either of these particles. The effective width thus defined can be substantially larger than the width of the boundary layer defined for the atomically clean interface between metal grains [45]. Experimental evidence of the wider grain boundary can be seen e.g., in the micrograph of a polycrystalline metal obtained in [46]. The estimated effective grain boundary width (δ_{GB}) will be used for the phase-field modelling.

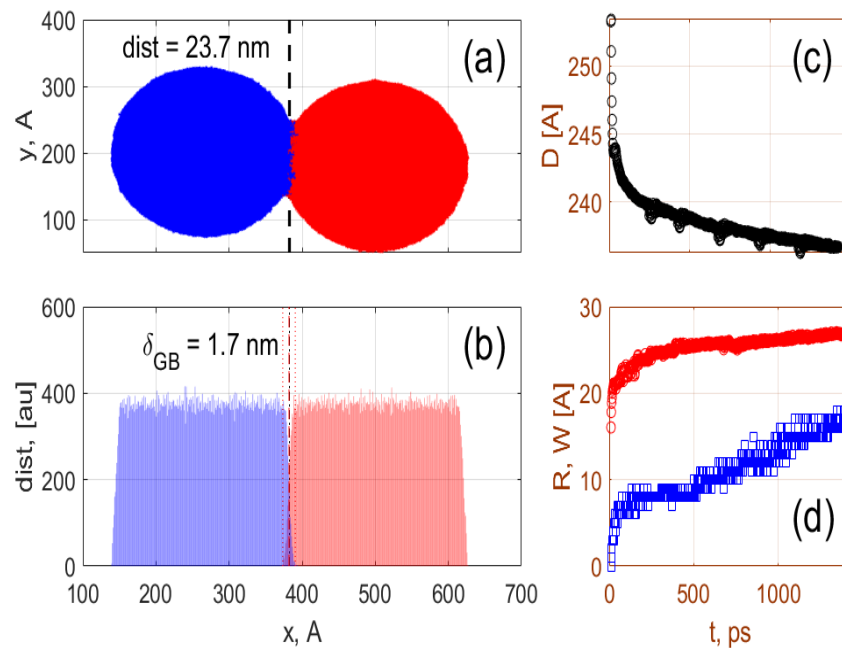


Figure 2. (a) Two interacting particles with the interface shown by the vertical dashed line. (b) Distribution of titanium atoms in two particles along the x coordinate within a cylinder of radius 5 nm whose axis passes through the centres of both particles. The interface between the particles is shown by the vertical dashed line. (c) Distance between particle centres as a function of time. (d) The effective grain boundary width (blue squares) and neck radius (red circles) as a function of time. The δ_{GB} is shown by vertical dash-dotted red vertical lines.

To analyse the diffusion process underlying the sintering, the trajectories of atoms that arrive in the boundary layer are tracked backwards in time, using the “prehistory approach” [47]. The corresponding trajectories of the Ti atoms forming the grain boundary structure are shown in Figure 3. The drift and diffusion coefficients of the atoms were calculated using a standard approach [48]. The trajectories of $N_{t1} = 3460$ and $N_{t2} = 4450$ Ti atoms were followed within the left and right particles, respectively. A small subset of these trajectories is shown in Figure 3. Each trajectory $\{r^i(t_1), \dots, r^i(t_{N_s})\}$ has length $N_s = 2300$ and sampling times t_j with time step $\Delta t = 0.4$ ps.

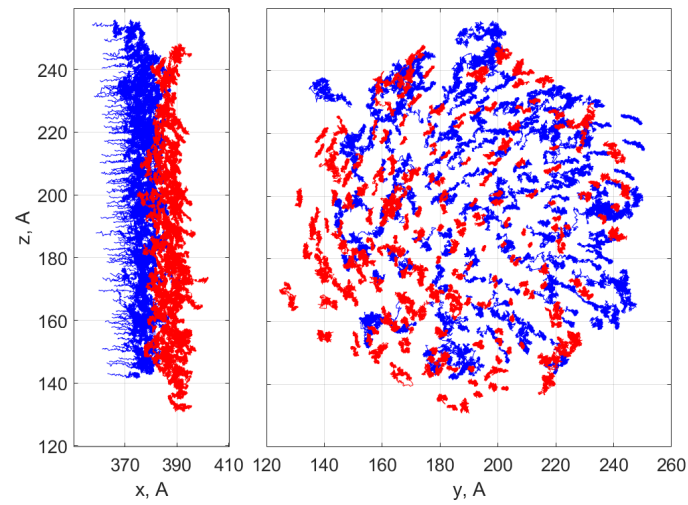


Figure 3. A subset of sampled atomic trajectories. **(left)** xz -view of trajectories of Ti atoms within the grain boundary layer after 1 ns of simulation. **(right)** yz -view of the same trajectories. The color coding is the same as in Figure 2: red trajectories belong to the right particle while blue correspond to the left particle.

Following this approach [48] the drift velocities ($\{a_x, a_y, a_z\}$) are found as

$$a_\alpha \approx \frac{1}{Nt} \sum_{i=1}^{Nt} \sum_{j=1}^{N_s-1} \frac{\alpha_{j+1}^i - \alpha_j^i}{\Delta t} \quad (1)$$

where $\alpha \in \{x, y, z\}$. Similarly, the diffusion matrix $D_{\alpha\beta}$ where $\alpha, \beta \in \{x, y, z\}$ is

$$D_{\alpha\beta} \approx \frac{1}{Nt} \sum_{i=1}^{Nt} \sum_{j=1}^{N_s-1} \frac{(\alpha_{j+1}^i - \alpha_j^i)(\beta_{j+1}^i - \beta_j^i)}{2\Delta t}. \quad (2)$$

Note that Equations (1) and (2) correspond to the values of drift and diffusion averaged in time over the atom trajectories that form the grain boundary at 1 ns and therefore should be considered as being order of magnitude estimates. It appears that MD simulations substantially overestimate the drift coefficient as $a \approx 70$ mm/s, while providing reasonable values for the diffusion coefficient with values ranging from $D_{surf} \approx 8 \times 10^{-10}$ m²/s to $\approx 1.6 \times 10^{-9}$ m²/s. The overestimation of the drift coefficient is probably related to the unaccounted rotation of the system around the axis of symmetry that connects the centres of the particles, which can be noticed in Figure 3 (right).

Importantly, MD simulations provide estimation for another key quantity of the system—the effective grain boundary width δ_{gb} —that will be used below to estimate sintering stress and sintering time in the phase-field model. It can be seen from the Figure 2 that δ_{gb} depends on time and quickly becomes $\gtrsim 10$ Å after approximately 0.5 ns of simulations of the particles with diameter $D = 24$ nm. It can also be seen that the width of the grain boundary is closely related to the geometry of the neck and can be expected to scale nearly linearly with the radius of the particle. It may be expected, therefore, that δ_{gb} is of the order of 1.0 μ m for particles of micron size.

The latter inference may clarify the situation in phase-field modelling of sintering. In the latter theory (see below) it is often assumed that the actual value of the δ_{gb} is ≈ 1.0 Å. Because this value is unsuitable for phase-field simulations, it is, therefore, re-scaled to 1.0 μ m on the assumption that such re-scaling does not change the dynamics of the model. However, this assumption is incorrect and is also unnecessary: it has been shown above that 1.0 μ m is a natural value of grain boundary width for the particles whose diameter is ~ 10.0 μ m.

The main results of this section that will be used for the estimation of the sintering stress and microstructure evolution include estimations of the important sintering parameters. It was shown that the grain boundary width δ_{gb} is of the order of $\sim 1.0 \mu\text{m}$ for particles of diameter $\sim 30 \mu\text{m}$, while the value of the surface diffusion coefficient D_{surf} was estimated to be in the range $\approx 8 \times 10^{-10} \text{ m}^2/\text{s}$ to $1.6 \times 10^{-9} \text{ m}^2/\text{s}$, while drift coefficients were significantly overestimated due to unaccounted rotation of the samples around the axis of symmetry. Molecular dynamics can evidently provide important insights into the mechanism of diffusion and can yield estimated values of the diffusion coefficient and grain boundary width. These parameters are also important for other theories including those of Coble [5] and Wakai [49], and for the master sintering curve method [50]. At present MD has a number of weaknesses, mainly related to the limited computing power [19] available. The size of the particles is limited to 30 nm in diameter and the time of simulations is of the order of 100 ns. However, it is expected that the MD will be able to handle larger numbers and diameters of particles in the near future due to ongoing hardware and algorithms development.

3. Microstructure Evolution

One of the most important issues in modelling sintering processes relates to the formation and growth of grains [7]. Sintering can be divided into four stages [7]: (i) contact formation, when weak atomic forces hold particles together prior to sintering; (ii) neck growth, when each contact enlarges without interaction with neighbouring contacts; (iii) pore formation, where neighbouring necks grow and interact to generate a network of pores; (iv) pore closure, where discrete pores are formed.

Scanning electron microscopy (SEM) provides deep insight into the evolution of the microstructure during these sintering stages, see, e.g., the SEM images of Ti6Al4V samples prepressed at 500 MPa and sintered at low temperatures shown in Figure 4. Results are shown for three different particle sizes (0–20, 20–45, and 45–75 μm) and two different sintering temperatures (900 $^{\circ}\text{C}$ and 1260 $^{\circ}\text{C}$). The heating rate in these experiments was 25 $^{\circ}\text{C}/\text{min}$ and the holding time was 1 h. A number of important features can be seen in the figure.

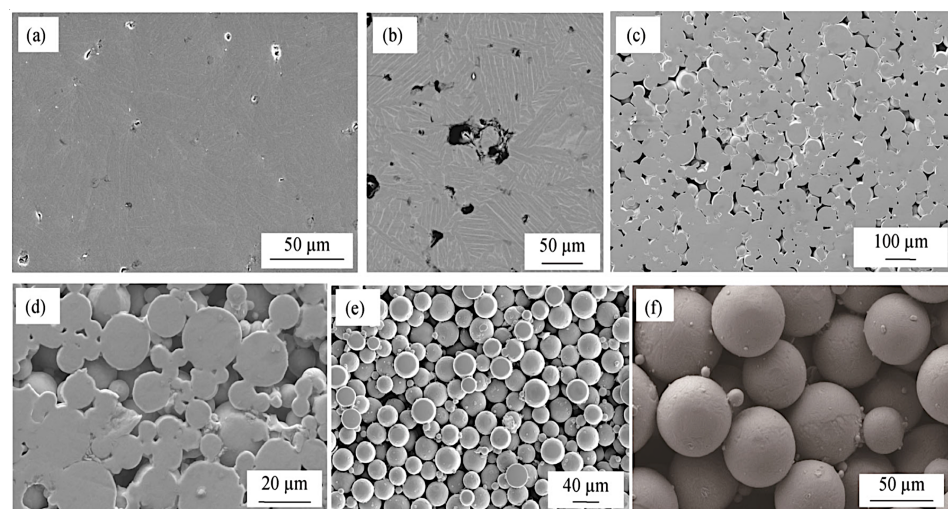


Figure 4. SEM micrographs of samples sintered at 1260 $^{\circ}\text{C}$ with particle diameters of (a) 0–20 μm , (b) 20–45 μm , and (c) 45–75 μm ; sintered at 900 $^{\circ}\text{C}$ for (d) 0–20 μm , (e) 20–45 μm , and (f) 45–75 μm . Reprinted with permission from Springer Nature Customer Service Centre GmbH: Springer, International Journal of Minerals, Metallurgy, and Materials [6].

First, note the strong dependence of the sintering results on the temperature. In particular, samples with particle sizes 0–20 μm sintered at 1260 $^{\circ}\text{C}$ are in the final sintering stage (iv), while samples sintered at 900 $^{\circ}\text{C}$ are still in transition from stage (ii) to stage (iii).

Samples with particle sizes 45–75 μm sintered at 900 $^{\circ}\text{C}$ are at the stage of green samples in transition to stage (i), while the samples sintered at 1260 $^{\circ}\text{C}$ are in transition from stage (iii) to stage (iv). These results are to be expected because sintering is governed by diffusion processes that depend exponentially on temperature.

Secondly, the results indicate that the sintering rate depends strongly on particle size. This observation can at least partially explain the overestimation of the sintering rate observed for nanoparticles in molecular dynamics simulations discussed in Section 2.

The set of states shown in Figure 4a–f also provides a good illustration of the different sintering stages, starting from the initial state (f) of nearly intact spherical particles, following to the initial necking state (e) where nearly intact spherical particles are weakly linked by necking, then to the final necking state (d) when the particles begin the transformation into the grains, followed by the grain growth (c) and pore shrinkage (b) to the final stage (a). This evolution is to a large extent generic, as discussed, e.g., in [7].

It is exactly this set of nonlinear transformations of the microstructure which is difficult to model. The phase-field method [14–16,51] has emerged as a powerful and flexible quantitative solution to this problem, including modelling the evolution of microstructure and the physical properties of metal powder on the mesoscale. Within this approach the evolution of the microstructure is defined in terms of the free energy F of the system defined as

$$F = F_{bulk} + F_{int} + F_{el} + F_{th} + F_{ext},$$

where the terms correspond respectively to the bulk free energy F_{bulk} , interfacial energy F_{int} , elastic strain energy F_{el} , energy terms due to thermal field F_{th} , and external field F_{ext} .

Within this approach, a set of phase-field variables is used that are continuous functions of time and spatial coordinates. A distinction is made between conserved and non-conserved variables. Conserved variables are typically related to the local composition. Non-conserved variables usually contain information on the local (crystal) structure and orientation. Order parameters and phase-fields are both non-conserved variables that are used to distinguish coexisting phases with different structures. The order parameters η_i refer to crystal symmetry relationships between coexisting phases [52]. Phase fields are phenomenological variables used to indicate which phase is present at a particular position in the system. In a system with N components, each having the number of moles n_i ($i = 1 \dots N$), the following conservative variables can be used [51]: mole fraction x_i and molar concentration c_i of i -th component

$$x_i = \frac{n_i}{n_{tot}}, \quad c_i = \frac{n_i}{V} = \frac{x_i}{V_m}$$

where $n_{tot} = \sum n_i$ is the total number of moles in the system, V_m the molar volume and V the total volume of the system.

3.1. Model Equations

In the phase field approach the microstructure evolution for variables n_i and c_i is modeled by a set of coupled Cahn–Hilliard (CH) and Allen–Cahn (AC) phase-field equations

$$\frac{\partial c_i}{\partial t} = \nabla \cdot M_i \nabla \left(\frac{\partial f_{loc}}{\partial c_i} + \frac{\partial E_d}{\partial c_i} - \kappa_{c,i} \nabla^2 c_i \right) \quad \text{and} \quad \frac{\partial \eta_j}{\partial t} = -L \left(\frac{\partial f_{loc}}{\partial \eta_j} + \frac{\partial E_d}{\partial \eta_j} - \kappa_{\eta,j} \nabla^2 \eta_j \right). \quad (3)$$

These equations are derived from the free energy functional F of isothermal sintering of metal particles [15,53]

$$F = \int \left[f_0(c, \eta) + f_{el}(c, \eta) + \frac{\kappa_c}{2} |\nabla c|^2 + \frac{\kappa_\eta}{2} |\nabla \eta|^2 \right] dV \quad (4)$$

with the internal phase-field free energy given by

$$f_0(c, \eta_i) = Ac^2(1-c)^2 + B \left[c^2 + 6(1-c) \sum_i \eta_i^2 - 4(2-c) \sum_i \eta_i^3 + 3 \left(\sum_i \eta_i^2 \right)^2 \right] = Ah(c) + Bg(c, \eta). \quad (5)$$

In Equation (3), A and B are constant parameters with units of e/l^3 , and κ_c and κ_η are coefficients of the surface and grain boundary energy gradients with units of e/l

$$A = \frac{(12\gamma_s - 7\gamma_{gb})}{\delta}; \quad B = \frac{\gamma_{gb}}{\delta}, \quad \kappa_c = (2\gamma_s - \gamma_{gb})\delta; \quad \kappa_\eta = \gamma_{gb}\delta; \quad (6)$$

γ_s and γ_{gb} are the surface and the grain boundary energies, δ is the grain boundary width. Note that the choice of the grain boundary width in the phase-field method is a subject of continuing discussion. E.g., in the work [16,54] the δ_{GB} is taken of the order of 1 nm that corresponds to the boundary layer of atomically clean interface between metallic grains. On the other hand δ_{GB} is often assumed to be of the order of the mesh size (i.e., $\sim 1 \mu\text{m}$) [51,55] or to have intermediate value, e.g., 60 nm [25] The results of the MD simulations discussed in the previous section will be used to estimate the effective width of the boundary layer δ_{gb} , which is shown to be of the order of $1 \mu\text{m}$. This value was used in the phase-field calculations below.

M and L are CH and AC mobilities with units $(l^2\text{mol})/(et)$ and $l^3/(et)$, respectively. M is calculated from the diffusion coefficients as [15]

$$M = M_{vol}\phi(c) + M_{vap}[1 - \phi(c)] + M_s c(1-c) + M_{gb} \sum \eta_i \eta_j \quad (7)$$

where $\phi(c) = c^3(10 - 15c + 6c^2)$ and M_{vol} , M_{vap} , M_s , and M_{gb} are respectively the coefficients for atomic mobility in solid bulk, vapour, along the surface, and along the grain boundary given by

$$M_i = \frac{D_i V_m}{k_B T}$$

with

$$D_{vol} = D_{vol}^0 e^{-\frac{Q_{vol}}{k_B T}}; \quad D_{vap} = D_{vap}^0 e^{-\frac{Q_v}{k_B T}}; \quad D_s = D_s^0 e^{-\frac{Q_s}{k_B T}}; \quad D_{gb} = D_{gb}^0 e^{-\frac{Q_{gb}}{k_B T}}, \quad (8)$$

where D_i^0 and Q_i are the corresponding diffusion coefficients and activation energies, k_B is the Boltzmann constant and T is the temperature.

A nondimensional form of the AC and CH equations is [56]

$$\frac{\tau_0 \partial \eta_j}{\partial t} = - \left(\frac{\partial}{\partial \eta_j} g(c, \eta) + \frac{\partial E_d/B}{\partial \eta_j} - \left(\frac{\delta}{l^*} \right)^2 \nabla^2 \eta_j \right). \quad (9)$$

$$\frac{\tau_0 \partial c}{\partial t} = \nabla \cdot \left(\frac{DV_m}{Lk_B T l^{*2}} \right) \nabla \left(\frac{\partial}{\partial c} \left[\frac{12\gamma_s - 7\gamma_{gb}}{\gamma_{gb}} h(c) + g(c, \eta) \right] + \frac{\partial E_d/B}{\partial c} - \frac{2\gamma_s - \gamma_{gb}}{\gamma_{gb}} \left(\frac{\delta}{l^*} \right)^2 \nabla^2 c \right).$$

In the simulations the size of the 2D region is of the order 100×100 pixels corresponding to an area of $\sim 100 \times 100 \mu\text{m}^2$, $l^* \sim 1.0 \mu\text{m}$, the value of δ is taken as $\sim 1.0 \mu\text{m}$, which was shown in the previous part $\delta_{gb} \sim 1.0 \mu\text{m}$ to be a natural length scale of the problem. The mobilities are defined as

$$\tilde{M} = \left(\frac{MB}{l^{*2}} \right) \cdot \tau_0 = \left(\frac{3}{4} \frac{DV_m \gamma_{gb}}{\delta_{gb} k_B T l^{*2}} \right) \cdot \tau_0 \quad \text{and} \quad \tilde{L} = (LB) \cdot \tau_0 = \left(\frac{M_{gb} \gamma_{gb}}{\delta^2} \right) \cdot \tau_0.$$

Examples of parameter values for this problem are given by e.g., Biswas et al. [15] for tungsten, by Zhang [53] for Ti and Ni, by Wang [57] for TiAlV alloy, and by Ahmed [54] for CeO₂. In the present work the following model parameters were used: $A \sim 15 \times 10^9 \text{ J/m}^3$, $B \sim 1 \times 10^9 \text{ J/m}^3$, $\gamma_s \sim 2 \text{ J/m}^2$ and $\gamma_{gb} \sim 1 \text{ J/m}^2$, $\kappa_c \sim 3 \times 10^{-9} \text{ J/m}$, and $\kappa_\eta \sim 1 \times 10^{-9} \text{ J/m}$, $L \sim 3.6 \times 10^{-9} \text{ m}^3/(\text{J}\cdot\text{s})$ and intrinsic interface mobility $M_{gb} \sim 2.6 \times 10^{-15} \text{ m}^4/(\text{J}\cdot\text{s})$, cf. [57]. The diffusion mobility M given by Equation (7) usually relies on diffusion coefficients that are found experimentally. Values of the diffusion coefficients were also estimated by MD simulations, see Section 2. The molar volume of Ti was taken to be $V_m = 10.43 \text{ cm}^3/\text{mol}$ (or atomic volume $\Omega_m = V_m/N_A \sim 1.7 \times 10^{-29} \text{ m}^3$) and the relationship between L and the grain boundary mobility M_{gb} to be $L = 4/3(M_{gb}/\delta)$.

3.2. Mechanical Loading

To include the effects of external loading and gravity, the phase-field model needs to be coupled with elasticity. Such a coupling with the phase-field equations is usually introduced within the theory of structural transformations in solids [58]. The governing equation within the domain Ω and boundary $\Gamma = \Gamma_i \cup \Gamma_d$ can be stated as follows:

$$\begin{aligned} \nabla \cdot (\boldsymbol{\sigma} + \boldsymbol{\sigma}_0) + \mathbf{b} &= \mathbf{0} \text{ in } \Omega \\ \mathbf{u} &= \mathbf{d} \text{ in } \Gamma_d; \quad \boldsymbol{\sigma} \cdot \mathbf{n} = \boldsymbol{\iota} \text{ in } \Gamma_i \end{aligned} \quad (10)$$

where $\boldsymbol{\sigma}$ is the Cauchy stress tensor, $\boldsymbol{\sigma}_0$ is an additional source of stress (such as pore pressure), \mathbf{u} is the displacement vector, \mathbf{b} is the body force per unit volume including gravity, \mathbf{n} is the unit normal to the boundary, \mathbf{d} is the prescribed displacement on the boundary, and $\boldsymbol{\iota}$ is the prescribed traction on the boundary. The gradient of stress has units $\nabla \boldsymbol{\sigma} \left[\frac{\text{m}}{\text{m}^2 \cdot \text{s}^2} \right]$.

Within the theory [58] the elastic energy has to be added to the total free energy (4). For the elastic energy calculation, the elastic strain ($\boldsymbol{\epsilon}$) is computed from the displacements, and corresponding stresses ($\boldsymbol{\sigma}$) from Hooke's law; for further details see [16]. The resultant elastic free energy is of the form

$$f_{el} = \frac{1}{2} \int_V [C_{ijkl} \epsilon_{ij} \epsilon_{kl} - \sigma_{ij}^a \epsilon_{ij}] dr,$$

where the material stress response is described by the constitutive model, in which the stress is determined as a function of the strain $\boldsymbol{\epsilon}$, e.g., $\boldsymbol{\sigma} \sim (\boldsymbol{\epsilon} - \boldsymbol{\epsilon}_0)$, and $\boldsymbol{\epsilon}_0$ is a stress free strain. For example, the elasticity is assumed to be linear for small strains, i.e., $\boldsymbol{\sigma} = \mathbf{C}(\boldsymbol{\epsilon} - \boldsymbol{\epsilon}_0)$ where \mathbf{C} is the elasticity tensor. The model Equations (3)–(10) are solved in MOOSE Multiphysics [14,16].

3.3. Results

Numerical simulations of the particle sintering model given by Equations (3)–(10) are performed using phase-field and mechanics modules in the MOOSE Multiphysics [32] environment. The simulations were performed using 2D and 3D phase-field models of sintering.

Results of the 2D Simulations are shown for 23 particles in Figure 5 with zero gravity and periodic boundary conditions.

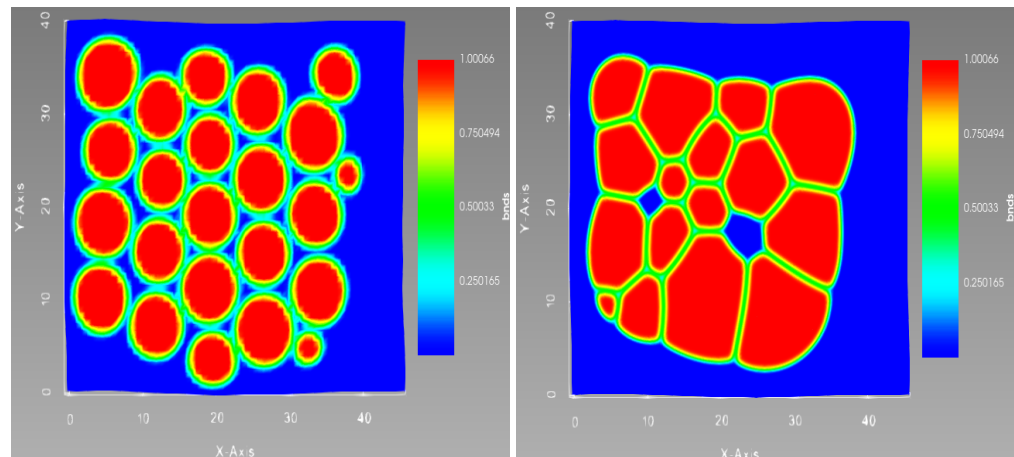


Figure 5. Results of the phase-field simulations of the microstructure evolution for 23 particles, in zero gravity, with periodic boundary conditions. **(left panel)** Initial distribution of the 23 “particles”. **(right panel)** Distribution of the metal particles in the end of the simulation time.

It can be seen that the phase-field model reproduces the transformation from particulate to dense granular structure of the samples shown in Figure 4c–f. This model also provides insight into the faults developed during such transformation, as shown in Figure 5 (right), which is consistent with the experimental observations [56]. The formation of the defects both between the particles inside the filament and between filaments can be reproduced by the model. In particular, open pores shown in Figure 5 (right) correspond to the open pores that can be seen in the Figure 4c. A set of interconnected open pores corresponds to the lack of fusion defects observed experimentally in [28]. The formation of such defects will depend strongly on the initial distribution of the particles, as will be further discussed in Section 4.

The 3D phase-field models can be further used to estimate the sintering stress and time scales. Results of the phase-field simulation of 3D sintering of metal particles are shown in Figure 6. The simulation domain was $V_0 = 27 \times 21 \times 12 \mu\text{m}^3$ and the mesh size was $40 \times 40 \times 30$. The dimensionless parameters used in the simulations were $A = 16.0$, $B = 1.0$, $L = 1.0$, $\kappa_c = 1.0$, and $\kappa_\eta = 0.5$, see also [15]. The preconditioned Jacobian Free Newton Krylov solution method was used with an initial time step of 0.001 and a growing factor of 1.1. Note that, at present, the number of particles in simulations is limited to just a few. To speed up the simulations, the mesh adaptation was excluded, accordingly, the results can be considered only as order of magnitude estimates. Yet, the simulations remain time-consuming, cf. [59]. An example simulations for 9 particles during 20 dimensionless time units took about 36 h, using 32 threads of the Threadripper 2990WX.

The evolution of the free energy and the internal boundary of this system are shown in Figure 7. It can be seen from the figure that initially round particles are transformed into grains with a number of grain boundaries similar to those observed experimentally in [60]. These results will now be used in the next section for estimation of the sintering stress.

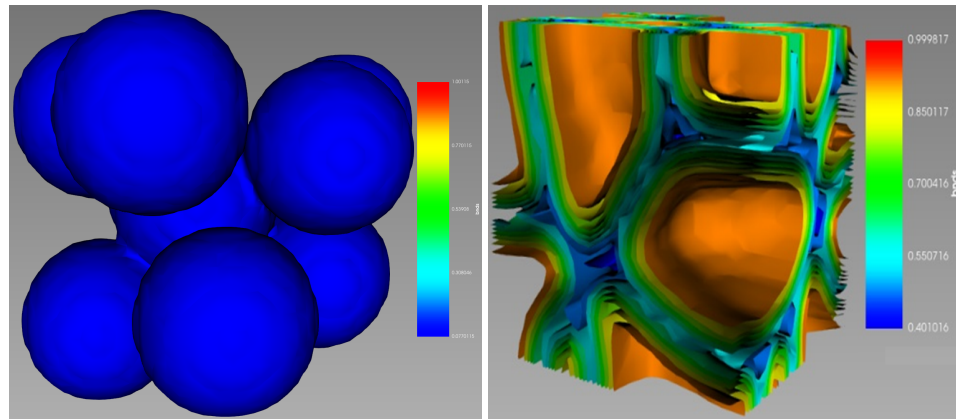


Figure 6. Results of the phase-field simulations of the microstructure evolution in 3D solid state sintering: **(left)** at initial time and **(right)** cross-sectional view after 24 time units.

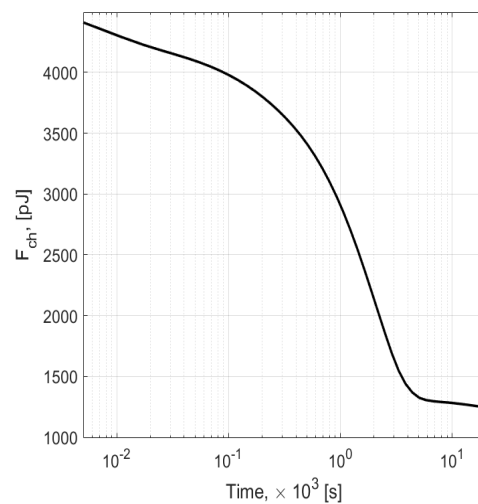


Figure 7. Results of the phase-field simulations of the chemical free energy as a function of time.

Sintering Stress

To estimate the sintering stress from the results of the PFM simulations, note that the corresponding pressure scale can be approximated by the Laplace pressure in the form [61,62] $P_L = \gamma_s/R_p$, where R_p is the mean particle radius and γ_s is the surface tension. For the $\gamma_s \sim 2 \text{ J/m}^2$ and $R_p \sim 10 \text{ }\mu\text{m}$ it can be shown that $P_L \sim 10^5 \text{ Pa}$. The sintering stress is in general defined [21,62] as

$$P_L = \frac{\partial F}{\partial V} \approx \frac{\Delta F}{\Delta V} \quad (11)$$

where F is the free energy and V is the volume occupied by the particles. The time evolution of the free energy is shown in Figure 7. Its shape correlates strongly with the shape of the shrinkage dependence on time shown in Figure 2 of Ref. [6], i.e., a nearly flat initial region followed by a sharp decay of the free energy F , corresponding to rapid shrinkage of [6]. Finally, a slow decay of the F is observed for large times, which again is strongly correlated with the slow shrinkage region observed in [6] for large times.

Such a strong correlation originates in the mechanism of sintering, which follows the four stages [7] listed at the beginning of Section 3 and illustrated in Figure 4. According to this mechanism, the initial rearrangement of particles at low densities leads to contact formation and necking, followed by independent neck growth. Necking and neck growth correspond to the sharp shrinkage and decay of the free energy.

Independent neck growth is followed by pore formation, and slow diffusion of pores to the sample surface. The pores occupy a relatively small volume of the sample. Their

diffusion is relatively slow and corresponds to the slow regions observed in shrinkage and decay of the free energy discussed above. To estimate the sintering stress, note that the change of the free energy ΔF in the Figure 7 is given in pJ, while the change of the particle's volume ΔV corresponds to the change of relative density of the particles from ~ 0.3 to ~ 0.96 of the simulation domain volume V_0 . This yields the following value for the sintering stress in (11): $P_{sint} \sim 6.7 \times 10^5$ Pa.

Another way to estimate the sintering stress is to notice that the initial free energy can be written in the form

$$F_{s,i} = \sum_{i=1}^{N_p} S_i \gamma_s,$$

where N_p is the number of particles, and S_i is the surface area of the i -th particle. For a crude estimation, the final free energy can be taken as zero, while analysis of the intermediate state can be done by assuming that all the particles have the same volume but their shape is changed to the space-filling polyhedra, cf. Figure 4c,d. Consider, for example, a truncated octahedron, for which volume V_{to} and surface area S_{to} are known as a function of the edge length a

$$V_{to} = 8\sqrt{2}a^3 \quad \text{and} \quad S_{to} = (6 + 12\sqrt{3})a^2.$$

This allows one to calculate $S_{to,i}$ for the metal particles and to estimate intermediate surface energy by noticing that all the particles are in full contact with each other

$$F_{s,f} = \frac{1}{2} \sum_{i=1}^{N_p} S_{to,i} \gamma_{gb},$$

where the factor $1/2$ is included to avoid double counting of the octahedron's surfaces.

The corresponding change in the volume of the system of particles ΔV can be found as above, which gives the following estimate for the sintering stress $P_L \approx 6.6 \times 10^5$ Pa.

To conclude this section it is pointed out that the phase-field model provides deep insight into the microstructure evolution of the system during sintering and can reproduce the transformation from particulate to dense granular structure of the samples, as observed in the experiments. It can also be used to estimate qualitatively the fault development during such transformations, which can then be compared with the experimental observations. 3D phase-field models can be used to estimate sintering stress and other parameters required for modelling the sintering of full-size parts. This model was applied to simulate the microstructure evolution in the cross-section of one filament. In 2D this approach allowed modelling of the sintering of a few tens of "particles" with diameters of the order of a few microns, on the time scale of hours. In 3D the number of particles had to be reduced to ten. The values of the sintering stress were estimated to be of the order 1 MPa. These results agree with experimental observations and can further be used for finite element modelling of the whole part.

Next, an approach is considered that can be used for modelling initial shrinkage in submodels that include tens of thousands of particles. This approach allows for particle resolution and provides estimates of the mass distribution in the sample that takes account of the filament layout and the initial rearrangement of the particles.

4. Discrete Particle Model

This section considers modelling of initial sintering stage within a framework of the discrete element method (DEM) [17–20] based on a new generalised viscoelastic model of sintering proposed in [17]. Within this method the translational and rotational dynamics of the particles are resolved by integrating [63] the Newton's equations of motion. For the i -th particle,

$$m_i \ddot{u}_i = F_i \quad I_i \dot{\omega}_i = T_i,$$

where u_i is the element's centroid displacement in a fixed (inertial) coordinate frame, ω_i the angular velocity, m_i is the element mass, I_i is the moment of inertia, T_i is the resultant moment about the central axes, and F_i is the resultant force including external forces such as gravity. The important component is the contact force F_c , which is divided into the normal and tangential sub-components, F_n and F_t , respectively $F^c = F_n + F_t$. The normal part of the contact force can be further divided into sintering F_s and viscous resistance F_v forces: Rojek et al. introduced the following approximation [19] to the normal component of the contact force

$$F_n = F_v + F_s = \frac{\pi a^4}{8D_{eff}} v_{rn} + \pi \gamma_s \left[4r \left(1 - \cos \frac{\psi}{2} \right) + a \sin \frac{\psi}{2} \right] \quad (12)$$

where v_{rn} is the normal relative velocity, r is the particle radius, a is the radius of the interparticle boundary, ψ is the dihedral angle, and γ_s is the surface energy. The effective diffusion is dominated by the grain boundary diffusion mechanism and can be approximated as

$$D_{eff} = \frac{D_{gb} \delta \Omega}{k_B T} \quad (13)$$

where D_{gb} is the grain boundary diffusion coefficient, δ is the width of the grain boundary, Ω is the atomic volume, k_B is the Boltzmann constant, and T is the temperature.

The constitutive relations take the form [19]

$$\dot{\sigma} = \mathbf{C} : (\dot{\boldsymbol{\varepsilon}}^e - \dot{\boldsymbol{\varepsilon}}^T - \dot{\boldsymbol{\varepsilon}}^v) + \mathbf{I} \dot{\sigma}^{sint} \quad (14)$$

where σ is the Cauchy stress tensor, \mathbf{C} is the elastic stiffness tensor, σ^{sint} is the sintering driving stress, and the strain rate $\dot{\boldsymbol{\varepsilon}}$ is decomposed into the elastic, thermal and viscous parts, $\dot{\boldsymbol{\varepsilon}}^e$, $\dot{\boldsymbol{\varepsilon}}^T$ and $\dot{\boldsymbol{\varepsilon}}^v$ respectively.

The DEM approach was used to model rearrangements of particles at the initial stage of sintering in realistic geometries and filament layouts. A discussion of some results of simulations is presented in the next section. The discrete element model of particle sintering was developed in KRATOS Multiphysics [33,34]. The contact forces [18] between two particles were modelled using the Hertz model with JKR cohesion [64] as a sum of elastic and viscous components. The elastic part assumes a linear force–displacement relationship

$$F^{elas} = k u_r$$

where u_r is the particle's penetration and k is the contact stiffness. The viscous component is assumed to be a linear function of the normal relative velocity v_{rn}

$$F^{visc} = c v_{rn}$$

and the viscosity coefficient c can be taken as a fraction ζ of the critical damping C_{cr} for the system considered

$$c = C_{cr} = \zeta \sqrt{\frac{k m_i m_j}{m_i + m_j}}$$

where m_i and m_j are the masses of two particles and k is an effective spring stiffness.

This model was used to analyse shrinkage as a function of the filament layout and gravity. The effect of these factors on nonlinear shrinkage was of particular interest, as was changes in the microstructure of the samples at the initial stage of sintering.

The effect of the filament layout on nonlinear shrinkage was simulated in a submodel of the NIST test artefact (see Figure 8) using the DEM Application in KRATOS [33,34]. The model of the artefact was sliced using Repetier-HOST v.2.1.6 slicer, see Figure 8a. Next, a small subsystem, the cylinder shown in Figure 8b, was selected for further analysis. Finally, sub-models of the cylinder with different filament layouts were constructed.

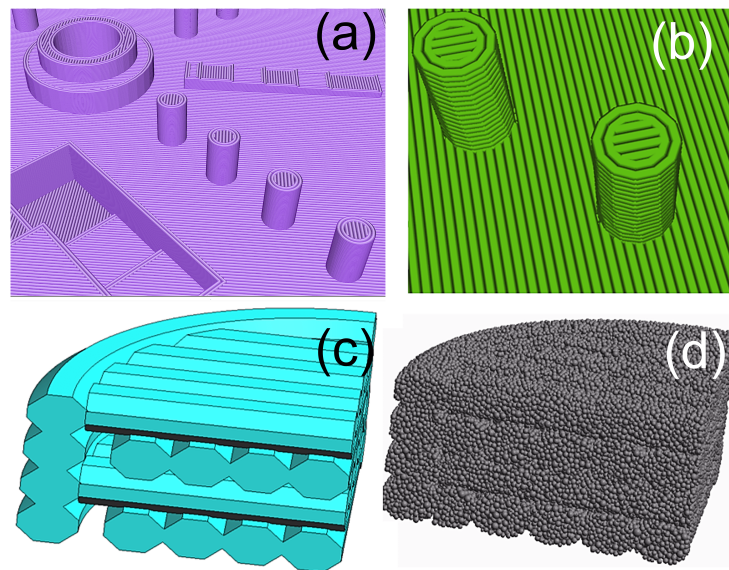


Figure 8. (a) Fragment of sliced NIST artefact for additive manufacturing. (b) Zoomed view of a small part of the artefact. (c) Geometry of the top few layers of the cylinder shown in figure (b) obtained in KRATOS DEM. (d) Discrete element model of the filaments in KRATOS DEM. The total number of spherical particles in the model $\approx 150,000$.

The sub-models were built in SALOME v9.3 [65] for two different filament layouts: (i) crossed layers and (ii) all layers are laid in the same direction. The STL files of sub-models were imported into KRATOS Multiphysics. Simulations were conducted using the DEM application. The resultant geometry for cross-layers and the final mesh for unidirectional layers are shown in Figure 8c,d, respectively. The material parameters chosen for the simulations are shown in Table 2.

Table 2. Parameters of some packing models.

Parameter Name	Parameter Value
Density ρ	4500 kg/m ³
Poisson ratio	0.3
Coefficient of restitution	0.2
Constitutive law	Hertz with JKR cohesion
Young's modulus, E	5×10^6 Pa
Cohesion E_c	1500 Pa
Gravity acceleration	9.8 m/s ²

The resultant shrinkages for unidirectional and cross layouts are compared in Table 3. The Young's modulus and cohesion used in these simulations were $E = 1.5 \times 10^6$ Pa and $E_c = 1500$ Pa respectively (other parameters are shown in Table 2). The default porosity was 56%. The total number of spherical articles in these simulations was $\sim 150,000$.

For example, the table shows the following shrinkage for the unidirectional layout (left half) in x -, y -, and z -directions: $L_{x,f}/L_{x,0} = 0.893$, $L_{y,f}/L_{y,0} = 0.884$ and $L_{z,f}/L_{z,0} = 0.754$. These results indicate that shrinkage in the horizontal plane is nearly the same in x - and y -directions while shrinkage in the z -direction is slightly larger. Similar results are obtained for crossed layout of the filaments. The corresponding shrinkage is: $L_{x,f}/L_{x,0} = 0.875$, $L_{y,f}/L_{y,0} = 0.878$ and $L_{z,f}/L_{z,0} = 0.826$ indicating that, for the crossed layout, shrinkage in all the directions is slightly smaller than for the unidirectional layout.

Repeating the simulations for this set of model parameters [56] revealed a weak dependence of the shrinkage on the filament layout. In most cases, the initial shrinkage

is smaller in the vertical and horizontal directions for cross-layout as compared to the unidirectional layout. This trend is more pronounced for an increased initial porosity. However, the dependence is weak and depends on model parameters such as Young's modulus, cohesion energy, and gravity. The latter strongly affects nonlinear shrinkage as will be discussed next.

Table 3. Results of simulations of shrinkage of the submodel of the NIST artefact with the following parameters: $E = 10^6$ Pa; $E_c = 500$ Pa; $\nu = 0.3$; restitution = 0.2; $t = 5$ s; porosity default; layout—uni (left) and cross (right).

$E = 1 \times 6$ Pa; $E_c = 500$ Pa; Default; Uni				$E = 1 \times 6$ Pa; $E_c = 500$ Pa; Default; Cross			
LY0	17.3	LZ0	12.34	LY0	15.9	LZ0	10.9
LYF	15.29	LZF	9.31	LYF	13.96	LZF	9.01
LYF/LY0	0.884	LZF/LZ0	0.754	LYF/LY0	0.878	LZF/LZ0	0.826
LX0	17.36	LX0	26.42	LX0	15.95	LX0	23.53
LXF	15.51	LXF	23.34	LXF	13.95	LXF	20.54
LXF/LX0	0.893	LXF/LX0	0.883	LXF/LX0	0.875	LXF/LX0	0.879

The effect of gravity was analysed by simulating two rectangular cuboids built of spherical metal particles. The latter are allowed to evolve under the action of gravity and interactive forces between the particles, on the ground, and in microgravity. The results of the simulations under normal gravity conditions are shown in Figure 9. These results are well reproduced. The cuboid dimensions in this sample are $0.5 \times 2.0 \times 0.3$ mm. The volumes of one cuboid and the spheres are $V_f = 0.3 \text{ mm}^3$ and $V_s = 0.13 \text{ mm}^3$ respectively. Accordingly the initial porosity is ~ 0.57 (fractional density ~ 0.43). It can clearly be seen from the figure that the initial shrinkage is strongly nonlinear. Shrinkage in the z -direction is ~ 0.22 while the sample practically does not shrink in the horizontal plane. The final porosity is ~ 0.42 (fractional density ~ 0.58), which corresponds approximately to the estimate of particle density in the filament in Figure 8. The lower the initial density, the larger the observed shrinkage in the z -direction. Note that the initial gap between the two filaments ~ 0.02 mm remains nearly intact to the end of the simulation. These results confirm the assumption that gravity on the ground can contribute significantly to the nonlinearity during the de-binding and earlier sintering stages when the initial fractional density of the samples is less than $\sim 55\%$.

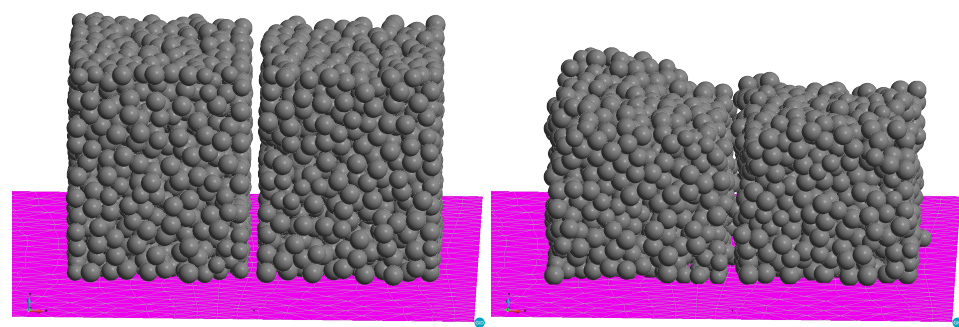


Figure 9. The effect of gravity on the initial shrinkage obtained in the DEM model. (left) initial state; (right) final state after 10 s of simulation time. The results of simulations are well reproducible.

To analyse the effect of microgravity, simulations of the same samples were performed under zero gravity conditions. The comparison of the samples' structure before and after shrinkage in microgravity is shown in Figure 10. The final fractional density of the samples after rearrangement of the particles under microgravity was found to be ~ 0.48 . One can see that under zero-G conditions there is no significant shrinkage in any direction as shown in Figure 10. Instead, agglomeration of the particles and the formation of large pores are

evident in the figure. Therefore, sintering under zero-G conditions may result in a higher probability of regions where there is a lack of fusion [27,28] as will be discussed in more detail in Section 5.

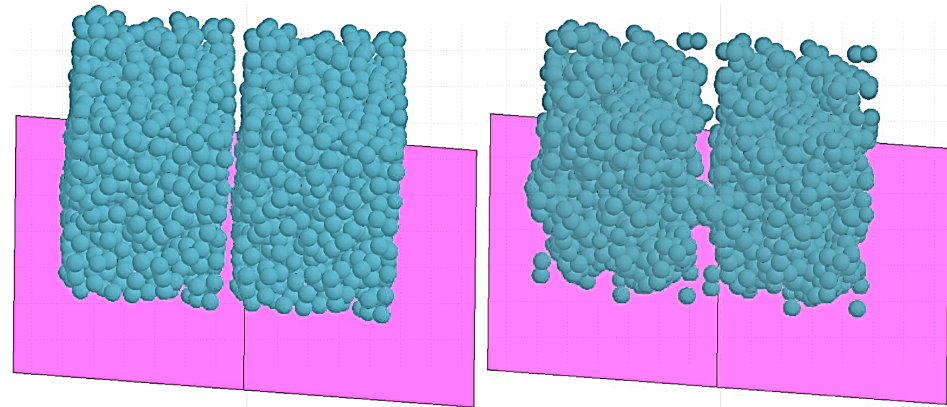


Figure 10. An example of the standard outcome of the simulations of the microstructure changes during debinding in zero gravity obtained using discrete element modelling of two rectangular cuboids: (left) before shrinkage and (right) after shrinkage.

Note that the discrete element method considered in this section provides important insight into the initial shrinkage of the filaments, but has some limitations both in accuracy and in the range of applications. Therefore, the DEM approach was mainly used to estimate the initial rearrangement of the particles, gravity-induced nonlinear shrinkage, and the spatial distribution of mass in the samples prepared in zero gravity. The model developed in KRATOS Multiphysics [33,34] allowed simulation of the translational and rotational motion of hundreds of thousands of interacting particles using the discrete element method. It was revealed that gravity is a major source of the strong non-linear shrinkage observed in experiments on the ground, while in zero-G, the shrinkage is only weakly depends on the filament layout and the spatial direction. It was also demonstrated that sintering in microgravity may result in the agglomeration of particles and increased risk of fault formation, including lack of fusion. These data were further used to develop a simple model of shrinkage and as input parameters in finite element modelling of sintering of the whole part.

5. Simple Model of Shrinkage

This section briefly summarises experimental results that can be used to correlate the structure of the sintered samples discussed in the previous sections with their density and mechanical properties.

5.1. Correlations

One of the key experimental relationships between the internal structure and mechanical properties of the sintered samples is given in the work by German [7] analysing correlations of the coordination number N_C with the fractional density f of the samples. He analysed over 113 reports to build experimental correlations for the coordination number, as shown in Figure 11 and introduced a simple functional form to fit these correlations

$$N_C = 2 + 11f^2. \quad (15)$$

The relationship (15) is plotted as the solid line in Figure 11 (left). It can be seen that experimental data derived from many sources can be well approximated by this equation. In particular, a transition from the $N_C \approx 6-8$, i.e., from the PSD approximately corresponding to simple cubic and body-centred cubic lattices, to $N_C \geq 12$, i.e., to the grains with approximately dodecahedral and tetrakaidecahedral structures happens above the fractional density ~ 0.65 . Such changes correspond to the transition from the initial to the

intermediate stage of sintering discussed at the beginning of Section 3, listed in Table 6.1 of Ref. [7] and illustrated in Figure 4 from (d) to (b).

Furthermore, the relationship (15) between f and coordination number allows one to relate N_C to all other key sintering parameters, including the pore diameter to grain size ratio d/G , the shrinkage, and the mechanical strength.

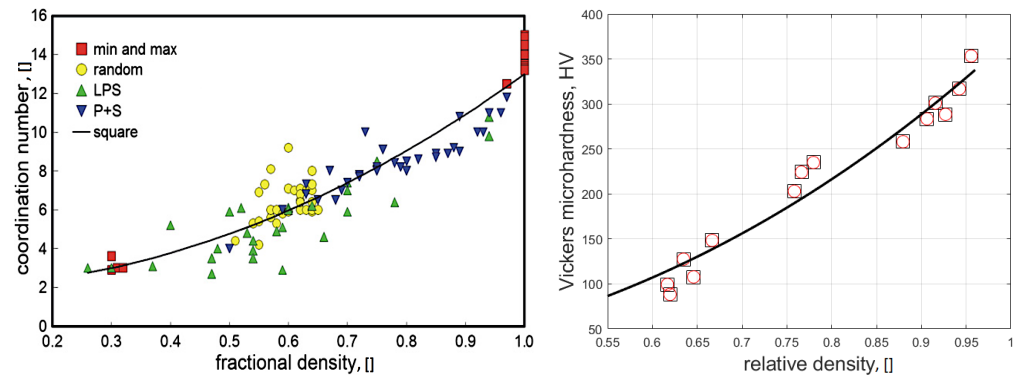


Figure 11. (left) Plot of the coordination number versus fractional density using tabulated data for minimum, maximum, random, compacted, sintered, and liquid phase sintered structures, including simulation data. The relation based on the square of the fractional density, according to Equation (15), is given by the solid line. Reprinted with permission from Elsevier and Copyright Clearance Center: Elsevier, Powder Technology [7]. Here LPS represents experimental data obtained using liquid phase sintering, while P+S corresponds to the experimental data obtained by pressing and sintering. “min and max” and “random” represent a mixture of experimental and simulated data. (right) Experimental data for microhardness as a function of relative density [6]. The solid line represents the results of fitting by correlations (19).

Indeed, all of the physical properties mentioned can be correlated with the fractional density. For example, at the earlier stages of sintering, the pore diameter to grain size ratio d/G can be related to the shrinkage as [6,66]

$$\frac{d}{G} = \left[\frac{\Delta l}{l_0} \cdot b \right]^{1/2} \quad (16)$$

where parameter $b \approx 3.6$, Δl is the change of the sample length and l_0 is the initial length in a given direction. At the same time, uniform shrinkage is related to the relative density as [66]

$$\frac{\Delta l}{l_0} = \left[1 - \left(\frac{f_{in}}{f_{fn}} \right)^{\frac{1}{3}} \right]. \quad (17)$$

The last two equations relate d/G to the initial and final fractional densities f_{in} and f_{fn} , respectively.

In addition, key mechanical properties of the sintered samples, such as microhardness, Young’s modulus, and yield stress, can also be correlated with the fractional density [6,67]. Experimental data for the sintered Ti-6Al-4V samples collected in [6,68,69] are used to illustrate the latter correlations. These data can be fitted using Ashby correlations [67] of the polynomial type

$$E = E_0 f^n \quad \text{and} \quad \sigma = \sigma_0 f^n. \quad (18)$$

The results of fitting are shown in Figure 12 with the following parameters: (i) $E_0 = 108.9$, $n = 5.9$; (ii) $\sigma_0 = 1050$ and $n = 3.8$. Similarly, the micro-hardness of the sintered Ti-6Al-4V samples can be correlated with relative density using Ashby type correlations

$$H = H_0 f^n. \quad (19)$$

The results of fitting are shown in Figure 11 (right) where the fitting parameters are $H_0 = 373.2$ and $n = 2.4$. It is concluded that both the main structural properties (including neck-to-grain size ratio and coordination number) and the key mechanical properties (such as microhardness, Young's modulus, and yield strength) of the sintered Ti-6Al-4V samples can be correlated with the fractional density f of the powder. Density is therefore one of the key fundamental properties of the samples that can provide a basis for developing a simple predictive model of nonlinear shrinkage, as will be discussed in more detail in the next section.

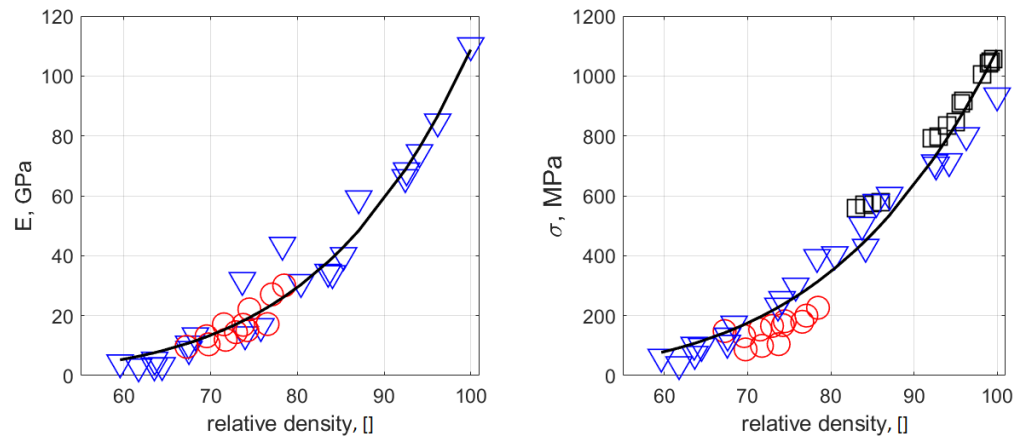


Figure 12. Mechanical properties of the sintered samples as a function of the relative density. The (left) panel shows experimentally obtained data for Young's modulus [6,69] and the (right) panel shows the experimental data for yield stress [6,68,69] as a function of the relative density in each case. The following symbols are used in the left panel \circ represent results from [68] and ∇ corresponds to [6]; while in the right panel ∇ —[6], \circ —[69], \square —[68]. The solid lines represent the results of fitting by correlations (18).

5.2. Estimation of Shrinkage

To introduce simple estimates of nonlinear shrinkage on the ground and in microgravity, the results of the previous subsection can be combined with the packing theory [70] and the experimentally observed shrinkage during metal additive manufacturing [11,27]. Samples with initial and final fractional densities in the range $f_{in} = 0.5$ – 0.6 and $f_{fn} = 0.9$ – 0.97 respectively, corresponding to the experimental observations [11,27], are considered as specific examples. The uniform shrinkages predicted by Equation (17) are shown in Figure 13. The values obtained are between 13 and 20%, in agreement with the experimental observations [11,27]. The smallest value ~ 0.13 is obtained for $f_{in} = 0.6$ and $f_{fn} = 0.9$, while the largest value ~ 0.2 is obtained for the densities $f_{in} = 0.5$ and $f_{fn} = 0.97$.

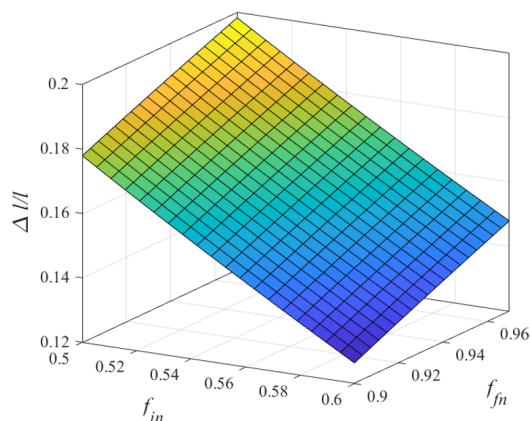


Figure 13. Shrinkage as a function of initial f_{in} and final f_{fn} densities according to correlations given by Equation (17).

Nonlinear shrinkage can be incorporated into the model by noting that one of the major factors affecting dimensional shrinkage during sintering is gravity [27]. It may be conjectured that the effect of gravity strongly depends on the density of the samples because for sufficiently small densities the powder behaves as a suspension [71], whose viscosity is a strongly nonlinear function of the density [72,73]. It is expected that a sharp transition from a polymer random-coil-like behaviour to true hard-sphere behaviour occurs for the fractional densities in the range from ~ 0.4 to ~ 0.6 [72,73]. Above these values of f both the viscosity and yield stress [71] may sharply increase. It is also expected that the gravity effect is most pronounced during debinding and at the earlier stages of sintering due to the agitation of metal particles.

The thermal agitation during debinding may therefore work as an additional effective settling mechanism that can lead to nonlinear shrinkage with additional shrinkage in the direction of gravity. The smaller the initial fractional density, the stronger is the nonlinearity. Accordingly, the simplified model assumes that the shrinkage takes place in two steps: (i) at the first stage the sample shrinks from an initial density f_{in} to the intermediate density f_m along the z -direction (i.e., the gravity direction) due to thermal agitation; (ii) at the second stage uniform shrinkage from the intermediate relative density f_m to the final density f_{fn} takes place. During settling and sintering, the mass of the sample remains constant, so that

$$V_{in}f_{in} = V_m f_m = V_{fn} f_{fn}, \quad (20)$$

where V_{in} , V_m , and V_{fn} are the initial, intermediate, and final volumes of the sample.

Assuming for simplicity samples of cubic shape, with initial side lengths $x = y = z = 1$ cm, the changes of sample dimensions during the first stage of sintering (using $V_k = x_k y_k z_k$, where k stands for initial, intermediate, and final stage) are

$$x_m = x_{in}, \quad y_m = y_{in}, \quad z_m = z_{in} \frac{f_{in}}{f_m}.$$

i.e., there is no shrinkage in the horizontal plane, while shrinkage in the z -direction scales as $\frac{f_{in}}{f_m}$. Thus, during the first stage the sample shrinks linearly in the gravity direction and does not shrink in the horizontal plane.

The second stage corresponds to the uniform shrinkage with the following scaling factors

$$x_{fn} = x_m \left(\frac{f_m}{f_{fn}} \right)^{\frac{1}{3}}, \quad y_{fn} = y_m \left(\frac{f_m}{f_{fn}} \right)^{\frac{1}{3}}, \quad z_{fn} = z_m \left(\frac{f_m}{f_{fn}} \right)^{\frac{1}{3}},$$

or in the form of shrinkage

$$\frac{\Delta x}{x_{in}} = 1 - \left(\frac{f_m}{f_{fn}} \right)^{\frac{1}{3}}, \quad \frac{\Delta y}{y_{in}} = 1 - \left(\frac{f_m}{f_{fn}} \right)^{\frac{1}{3}}, \quad \frac{\Delta z}{z_{in}} = \left(1 - \frac{f_{in}}{f_m} \left(\frac{f_m}{f_{fn}} \right)^{\frac{1}{3}} \right), \quad (21)$$

where $\Delta x = (x_{in} - x_{fn})$ and the scaling factors during the first and second stages are $sc_1 = \frac{f_{in}}{f_m}$ and $sc_2 = \left(\frac{f_m}{f_{fn}} \right)^{\frac{1}{3}}$ respectively. For example, assuming $f_{in} = 0.54$, $f_m = 0.61$, and $f_{fn} = 0.93$ shrinkage in the z -direction may be estimated as $\sim 23\%$ and in x - and y -directions as $\sim 13\%$, which is close to the results of the non-linear shrinkage observed in the experiments [11]. The approximation (21) can be further improved by noticing that f_{in} and f_{fn} are in fact distributions that can be measured experimentally. At the same time the unknown value of the intermediate relative density f_m can be inferred using Bayesian inference.

Nonlinear shrinkage can be reduced by increasing the initial relative density to ~ 0.6 while preserving the flowability and printability properties of the powder. Similarly, the probability of fault formation in microgravity, such as lack of fusion, discussed at the

end of Section 4, can be reduced by increasing initial relative density. The issues related to fault formation may become even more severe in space, where the sintering temperature often has to be reduced below 1200 °C.

Some mitigation strategies based on earlier experimental observations, possibly leading to higher initial relative densities, will now be discussed.

5.3. Fault Mitigation

A number of approaches can be used to mitigate issues related to nonlinear shrinkage on the ground, and to fault formation in microgravity. They include (i) increasing the initial density; (ii) sintering for a longer time; (iii) modifying the binder system. For example, the initial density can be improved by mixing two-sized particle distribution [74–76]. In addition, one could increase the sintering time to compensate for a reduced sintering temperature. The holding time can be increased up to 8 h [77] to improve final density. It is also expected that the sintering can be speeded up by decreasing the particle size of the powder [6]. The final density can also be adjusted by modifying the binder chemistry [78]. In the latter study, polyethylene (PE), paraffin wax (PW), stearic acid (SA), and the palm oil derivative palm stearin (PS) were mixed homogeneously with powder and injected to produce green compact. Four combinations were studied: PE/PS and PE/PW/SA in a vacuum and in an argon atmosphere. It was shown that the sintering results depend significantly on the binder system, e.g., the highest density and strength were obtained for the PE/PS system in an argon atmosphere.

Another sensitive set of parameters affecting the sintering results is the concentration of impurities such as oxygen (O) and carbon (C) [79]. In particular, it was found that samples obtained using injection moulding and sintering at 1150 °C with ~0.14% of C and O possess the highest values of density and tensile strength, while samples sintered at 1200 °C with ~0.13% of C and O have the highest degree of ductility. The C concentration increases with rising sintering temperature, while the oxygen concentration decreases. Thus the effects of the O and C concentrations on the properties of sintered samples depend on the sintering temperature. The discussion above suggests a possible strategy for optimising the sintering of the Ti-6Al-4V alloy at 1150 °C. Steps to improve the quality of the samples include using: (i) a two-size distribution to increase initial powder density; (ii) smaller particle sizes to speed up the sintering process; (iii) increased sintering times of up to 8 h to obtain higher final density; (iv) control of the concentrations of carbon and oxygen in the alloy to maximise strength and density; (v) control of the binder system, noting that the strength and density can be maximised using PE/PS system in an argon atmosphere. Note that the above steps require very delicate tuning, and extensive experimental testing, and may be demanding in terms of time and resources.

The developed above simple model of sintering is relying on experimentally observed correlations, the theory of packing of spherical particles, and results of modelling shrinkage within the DEM. The density of sintered samples was used as the key system parameter correlated to the microstructure and mechanical properties of the samples. It was shown that below threshold density ~0.5, the metal powder can behave as a suspension of particles demonstrating nonlinear shrinkage in the gravity direction while above this threshold density the system shrinkage is nearly uniform. It was further shown that in zero-G, low initial density may result in the agglomeration and a higher probability of faults. To reduce the nonlinearity and improve the quality of the samples in microgravity, it was suggested to maintain the initial density as close as possible to the threshold value by e.g., using a two-sized distribution of the initial powder density, reducing particle sizes, increasing sintering time, controlling the concentration of carbon and oxygen in the alloy, and controlling the binder system.

Thus far, the grain boundary width and diffusion rates for sintering particles have been estimated by use of molecular dynamics, microstructure evolution dynamics, free energy as a function of volume, and sintering stress for a limited number of particles based on a phase-field model, and the initial redistribution, shrinkage, densities and shrinkage for

tens of thousands of particles have been estimated by discrete element modelling. Sintering of the whole part will now be considered.

6. Macroscopic Modelling of Sintering

Modelling shrinkage for the full-size parts was performed using the continuous finite-element method in commercial software COMSOL Multiphysics[®] [35]. In the simulations, the model parameters were kept close to those used experimentally in sintering Ti-6Al-4V alloy [56], which are also consistent with the simulations of the previous sections. Powders of this metal can be combined e.g., with some polymer mixtures to form feedstock for fused deposition modelling. Importantly, the softening temperature of compatible binder materials must be substantially lower than the melting temperature of the metal powder enabling filament printing through an extrusion method with subsequent debinding and sintering stages as described in the introduction, see also [4,56].

The simulations used typical structural parameters for the modelled material, noting that the green part was produced by printing filaments. Two different powders were considered, both coarse and fine [56,80]. It was further assumed that thermal debinding was achieved using a heating rate of 1–2 °C/min with 3 h holds at three different temperatures between 200 °C and 500 °C in low pressure to produce the brown part. Subsequently, the brown part underwent the 3 h sintering process at temperature above 1200 °C in a low pressure environment.

To simplify modelling it is assumed that thermal debinding of the green part was performed without shrinkage and collapse of the structure. The shrinkage of the sintered part was considered at the sintering stage. In this case a large fraction, e.g., 40%, of the sample volume after debinding is an empty space. Some residual binder (a backbone) may still be present until sintering starts to keep the brown part from disintegrating in zero gravity. Thus the initial stage may involve removal of the residual binder, necking and strong adhesion among the adjacent particles, causing the shrinkage of the part by ~10%: see the previous section. Subsequent sintering takes place in a vacuum or in an inert gas [81].

After thermal debinding, only a small amount of residual backbone binder is left, mostly located in inter-particle pockets. In this case two mechanisms of sintering could be considered. The first one is due to sintering stress induced by the residual binder, and the second is due to shrinkage of the solid continuum. The first mechanism is due to viscoelasticity and creep behaviour. These phenomenological mechanisms will now be used to provide qualitative results for sintering and shrinkage.

6.1. Equations for Modelling Metal-Fused Filament Fabrication Process

The rheological theory of sintering developed by Skorohod [82] is based upon the phenomenological concept of the generalised-viscous flow of porous bodies. These ideas were further extended by Olevsky [21,22] by including, in particular, relationships between rheological parameters (such as bulk, shear viscosity and the effective sintering stress) and deformation of a viscous porous body under sintering.

Two stages of shrinkage are considered: debinding of the backbone polymer at a temperature close to sintering and the sintering itself. In addition, some properties of the sample obtained by metal fused filament fabrication (mf3) will be modelled. Dimensional change during the “mf3” process, shrinkage or swelling, can be predicted from continuum mechanics. During the debinding stage, the binder is burned out and removed from the furnace chamber, while the pores are filled by air or inert gas. The corresponding solid system transformation is modelled by solving systems of coupled continuous equations for solid state media, including for diffusion, and heat transfer. In addition, an account is taken of binder diffusion activated by temperature and the medium changes during debinding.

The corresponding dimensional changes are the result of changes in viscosity and the sintering stress. Because experimental parameters for these processes are not known,

phenomenological parameters introduced on the basis of the underlining physics are used instead.

In the simulations, the Ti-6Al-4V metal powder bound by the polymer subsystem is modelled as a continuous medium. The goal is to determine the shrinkage after the two stages of debinding and sintering. It is assumed that in the final stage of sintering the density of voids corresponds to the experimentally observed value of $\approx 5\%$. It is further assumed that the main shrinkage happens during the sintering of the metal part. In the next subsection, the modelling results are considered in more detail.

6.2. Constitutive Relations for Olevsky Model

The material response to loading and deformation is modelled using elastic σ_{el} and viscous σ_{vs} components, cf. Section 4,

$$\sigma_{el} = E\varepsilon \text{ and } \sigma_{vs} = \eta\dot{\varepsilon},$$

where σ is stress, ε is strain, E is a Young's modulus, and η is a viscosity. There are two different viscoelastic models to consider: (i) the Maxwell model

$$\dot{\varepsilon} = \dot{\sigma}/E + \sigma/\eta, \quad (22)$$

consisting of a spring term and a dashpot term placed in series where the first part is an elastic law and the second term is a creep; (ii) the Voigt–Kelvin model

$$\sigma = E\varepsilon + \eta\dot{\varepsilon}. \quad (23)$$

representing a solid undergoing reversible, viscoelastic strain. The constitutive Equation (22) leads to Riedel's model [83], while Equation (23) leads to the generalised Olevsky model [21,22]. The strain rate in the phenomenological sintering model consists of the equivalent elastic strain rate $\dot{\varepsilon}^e$, thermal strain rate $\dot{\varepsilon}^T$, and creep strain rate $\dot{\varepsilon}^{cr}$, cf. Equation (14). It is the last term that is responsible for sintering.

Olevsky's constitutive model [21] is given by the equation

$$\sigma_{ij} = 2\eta(\varphi\dot{\varepsilon}'_{ij} + \psi\dot{\varepsilon}_{ij}) + P_L\delta_{ij}, \quad (24)$$

where η is the apparent viscosity of the porous body skeleton, P_L is the effective sintering stress, and δ_{ij} is the Kronecker symbol. φ and ψ are the coefficients of effective shear and bulk moduli, respectively

$$\varphi = (1 - \theta)^2, \text{ and } \psi = (1 - \theta)^3/\theta. \quad (25)$$

Here porosity θ is defined as the ratio of the pore volume V_{pores} , to the total volume V_{total} . The sintering stress in the case of free sintering ($\sigma_{ij} = 0$) is

$$P_L = -2\eta\psi\dot{\varepsilon}_v, \quad (26)$$

where r_0 is the mean radius of powder particles, γ is the surface tension, and $\dot{\varepsilon}_v$ is a free volume shrinkage.

Equations (25) and (26), and the continuity equation for mass conservation $\dot{\varepsilon}_v = \dot{\theta}/(1 - \theta)$ yield

$$\dot{\theta} = -\frac{P_L}{\eta}\theta.$$

For time-independent coefficients, the solution of this equation is

$$\theta = \theta_0 \exp\left(-\frac{t}{\tau_{\text{sin}}}\right), \quad \tau_{\text{sin}} = \eta/P_L$$

where θ_0 is the initial porosity and τ_{sin} is the characteristic sintering time for continuum models. The effect of the sintering stress on the dynamics of porosity is illustrated in Figure 14. This dependence is a function of the viscosity and sintering stress. It can be seen from the figure that the higher the sintering stress the lower is the final porosity and the higher is the shrinkage. For the characteristic value $P_L \sim 10^6$ Pa and with a typical sintering time of ~ 3 h, the viscosity should be of the order 10^{10} – 10^{11} Pa·s. This implies that to reduce the sintering time the sintering temperature needs to be sufficiently close to the melting temperature in order to reduce the viscosity.

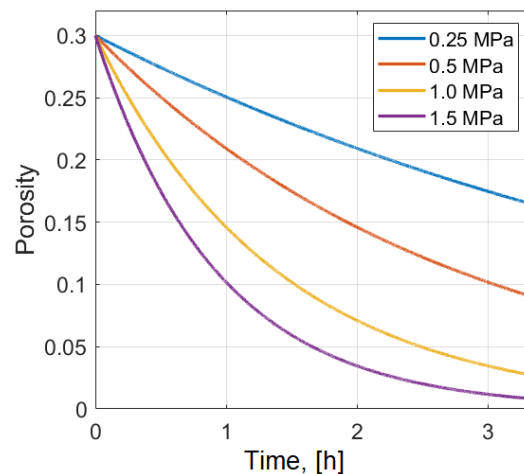


Figure 14. Dependence of the porosity on time at different values of the sintering stress. The initial porosity value is 0.3, $\eta = 0.5 \times 10^{10}$ Pa·s.

6.3. Simulation Results for the Olevsky Model

The commercial software COMSOL[®] [35] was used for simulation of the sintering process. In addition to the solid state structural module, the Domain ODEs and DAEs mathematics were used for porosity modelling. The viscoelastic properties were taken into account by using the Kelvin–Voigt approach. Some simulation experiments were undertaken to check limiting cases [56]. First, consider the case of zero gravity and no sintering stress, while keeping low viscosity 10^{10} Pa·s. In this case the initial porosity distribution ($\eta_0 = 0.3$) did not change after 3 h of sintering. Similarly, there were no changes in the displacement and stress since no external or internal stresses were applied. In the second numerical experiment gravity was applied. In this case the simulations exhibited small changes in porosity, displacement and stress. These changes depended on the value of the viscosity: the lower the viscosity, the larger were the changes.

For the sintering stress $P_L = 0.5$ MPa, viscosity $\eta = 10^{10}$ Pa·s, the initial porosity $\theta_0 = 0.3$, and sintering time ~ 3 h the porosity was reduced to 0.09 corresponding to shrinkage of about 7%. The distribution of the porosity in the vertical direction remained homogeneous in the absence of gravity and became slightly inhomogeneous ($\leq 0.1\%$) in the presence of gravity. The characteristic stress distribution (von-Mises invariant) displayed practically no stress in the structure. When the viscosity is reduced to 0.5×10^{11} Pa·s and the sintering stress is increased to 1.0 MPa, the shrinkage increases to about 13% in the vertical and lateral directions. The von-Mises residual stress remains sufficiently small.

In the next set of simulations the bottom constraint was introduced to keep the dimensions of the bottom pane fixed. Other parameters were $\theta_0 = 0.3$, $\eta = 1 \times 10^{11}$ Pa·s, and $P_L = 1$ MPa. The results of the simulations are shown in Figure 15. It can be seen from the figure that porosity was substantially reduced everywhere except in areas near the fixed corners of the structure. The high porosity at the corners was caused by the nonuniform stress distribution, which was sufficiently high at these locations. The shrinkage of the structure was about 10% in all directions, as shown in Figure 15b,c. The stress distribution is presented in Figure 15d–f. It can be seen that inhomogeneous stress S_y in the y -direction

is at least three orders of magnitude higher in the corners, which might lead to trapping of the porosity θ . The analysis is now extended by consideration of shrinkage in the presence of small amounts of backbone polymer.

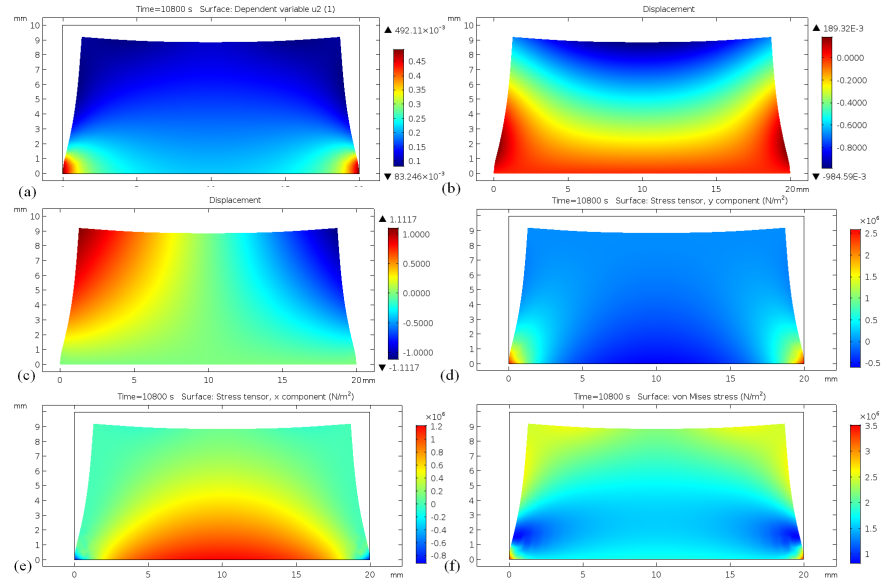


Figure 15. (a) Porosity distribution at the end of sintering time; (b) vertical displacement; (c) horizontal displacement; (d) stress distribution S_{yy} . (e) S_{xx} ; (f) von Mises. The initial porosity value is $\theta_0 = 0.3$, $\eta = 1 \times 10^{11}$ Pa·s, $P_L = 1$ MPa.

6.4. Constitutive Model for Backbone Polymer Debinding

To encompass in the model polymer debinding during sintering, it is necessary to take account of thermal diffusion of the binder material. The governing equations for an isotropic, homogeneous elastic solid medium with generalised thermodiffusion are [84,85].

$$\rho \frac{\partial^2 u_i}{\partial t^2} = \mu u_{i,jj} + (\lambda + \mu) u_{j,ij} + \beta_1 T_{,i} - \beta_2 C_{,i}, \quad i, j = 1, 2, 3 \quad (27)$$

where u_i are components of the displacement vector, T is the absolute temperature, C is the concentration of the diffusive material in the elastic body, λ and μ are Lamé's constants, ρ is the density, and β_1 and β_2 are material constants given by

$$\beta_1 = (3\lambda + 2\mu)\alpha_t, \quad \beta_2 = (3\lambda + 2\mu)\alpha_c \quad (28)$$

where α_t and α_c are the coefficients of linear thermal and diffusion expansion respectively.

The constitutive equation for the stress components σ_{ij} is

$$\sigma_{ij} = 2\mu\epsilon_{ij} + [\lambda\epsilon_{kk} - \beta_1(T - T_0) - \beta_2(C - C_0)]\delta_{ij}, \quad i, j, k = 1, 2, 3 \quad (29)$$

here T_0 and C_0 are the reference temperature and concentration, and ϵ_{ij} are the strain components given by:

$$\epsilon_{ij} = \frac{1}{2}(u_{i,j} + u_{j,i}), \quad i, j = 1, 2, 3$$

The diffusion of the polymer binder can be modelled as "moisture" transport governed by the diffusion equation:

$$\frac{\partial C}{\partial t} = D\Delta C \quad (30)$$

where the diffusion coefficient D is assumed to be of the activation type, cf. Equation (8)

$$D = D_0 \exp(-U/kT)$$

where U is the activation energy and k is the Boltzmann constant. The equations have to be complemented by the equation of thermal conduction

$$\frac{\partial T}{\partial t} = \kappa \Delta T, \quad (31)$$

where κ is the thermal conductivity coefficient.

The boundary conditions on the exterior faces of the part correspond to a flux of polymer concentration for Equation (30) and fixed temperature determined by the heating source. For sufficiently slow change of temperature, one can omit the solution of Equation (31) and assume that the sample follows the heating schedule quasi-statically. This thermally activates the diffusion of the binder at different stages and makes it possible to predict shrinkage.

Within the above formalism, shrinkage can be taken into account by introducing the strain concentration relation

$$\varepsilon = \beta M(C - C_0) \quad (32)$$

where β is the hygroscopic shrinkage (swelling) coefficient and M is the molar mass of degraded products of the residual backbone polymer.

To simplify the simulations it is assumed that shrinkage takes place during the debinding of the residual polymer. In this case, the formalism can be applied based on the solution of Equations (27)–(31). The parameters of the simulations were chosen as: $\beta = 10^{-3} \text{ m}^3/\text{kg}$; initial concentration $10^3 \text{ mol}/\text{m}^3$; diffusion coefficient $D = 4 \times 10^{-6} \text{ m}^2/\text{s}$; brown part density $3000 \text{ kg}/\text{m}^3$; Young modulus 10 GPa ; Poisson ratio 0.4 , for which the part undergoes volumetric shrinkage, consistent with experimental observations ranging from about 12% to 18% (cf. [11]) for final density ranging from 95% to 99.5% of the theoretical density. To estimate M in Equation (32), note that the molecular mass of the degraded polymer is determined by the polymer atoms.

The results of shrinkage simulations for this model are presented in Figure 16. It can be seen from the figure that, during sintering, the backbone polymer concentration changes by several orders of magnitude and experiences about 10% shrinkage. Similar simulations for a fixed boundary condition at the bottom demonstrate large residual stress leading to higher shrinkage in the vertical direction.

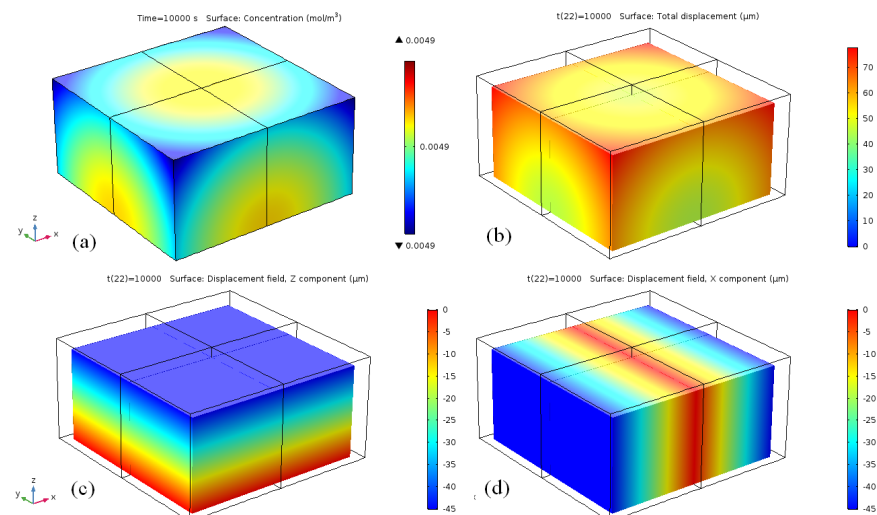


Figure 16. (a) Concentration of the backbone debinder after sintering; (b) total displacement; (c) direction z displacement; (d) x displacement. The parameters are $\beta = 10^{-3} \text{ m}^3/\text{kg}$, initial concentration $10^3 \text{ mol}/\text{m}^3$, diffusion coefficient $D = 4 \times 10^{-6} \text{ m}^2/\text{s}$, brown part density was taken as $3000 \text{ kg}/\text{m}^3$, Young's modulus 10 GPa , Poisson's ratio 0.4 .

This modelling approach is now applied to the analysis of shrinkage in the whole part, i.e., the entire NIST artefact; see also the CAD shown in Figure 8a. The results of this modelling are presented in Figures 17 and 18. It can be seen from Figure 17 that all the features of the CAD are reproducible and that the shrinkage is isotropic for the roller boundary conditions. The situation becomes more complex if the boundary condition is fixed at the bottom plane, see Figure 18. The final part is now deformed in the vertical direction and experiences inhomogeneous deformation in the X-Y plane. This means that, for the final part to have the correct dimensions, one has to introduce complex anisotropic compensation to the scales of the green part.

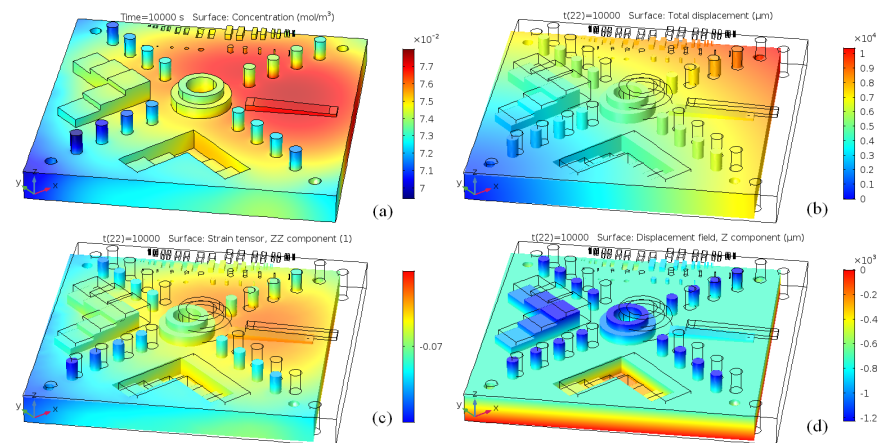


Figure 17. COMSOL simulations of: (a) the concentration of backbone debinder in the sintering part (after sintering); (b) total displacement; (c) directional strain; (d) displacement in the vertical direction. The parameters were $\beta = 10^{-3} \text{ m}^3/\text{kg}$, initial concentration 10^3 mol/m^3 , diffusion coefficient $D = 4 \times 10^{-6} \text{ m}^2/\text{s}$, brown part density was taken as 3000 kg/m^3 , Young's modulus = 10 GPa, Poisson's ratio = 0.4.

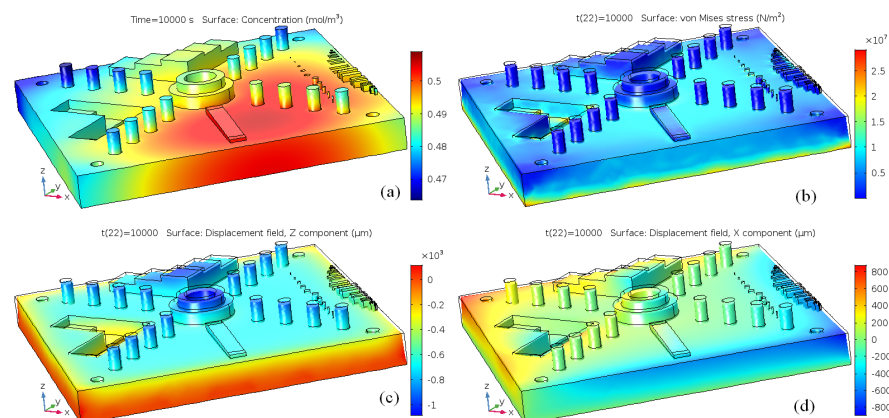


Figure 18. COMSOL simulations of: (a) concentration of backbone debinder in the sintering part (after sintering); (b) Von-Mises residual stress; (c) directional displacement vertically; (d) displacement in x. The parameters were $\beta = 10^{-3} \text{ m}^3/\text{kg}$, initial concentration 10^3 mol/m^3 , diffusion coefficient $D = 4 \times 10^{-6} \text{ m}^2/\text{s}$, brown part density was taken as 3000 kg/m^3 , Young's modulus = 10 GPa, Poisson's ratio = 0.4.

6.5. Nonlinear Shrinkage in Continuous Model

Analysis of anisotropic shrinkage within the continuous model above was performed using two formalisms—the Olevsky model and the debinding model based on thermal diffusion. Both models demonstrate shrinkage of the initial structure. In the absence of constraints at the bottom plane, they both exhibit nearly uniform shrinkage. Anisotropic shrinkage was observed for spatial variation of the model parameters. For example, in the

model based on thermal diffusion, the shrinkage rate of the brown part depends on the swelling coefficient, which is a phenomenological parameter and should be determined by experiment for each composition. In the Olevsky model there are two major parameters (viscosity and sintering stress) and the nonlinear shrinkage can arise as a result of spatial variation in either of these parameters. The latter variation can be determined using microscopic simulation discussed in Sections 3 and 4 or measured in an experiment.

For the low initial porosity ($\theta \leq 0.35$) considered in the simulations, the shrinkage is isotropic and independent of the initial porosity distribution unless an anisotropic sintering stress or swelling coefficient is prescribed. This result is expected because, at such a low porosity, the metal powder behaves as porous metal with uniform high viscosity and high sintering stress; see also discussion in Section 5.

On the other hand, for high initial porosity ($\theta > 0.4$) the powder behaves as a suspension of metal particles [71] that displays a very sharp dependence of sintering stress and viscosity on the porosity; see Section 5. In this case the presence of gravity may lead to significant nonlinear shrinkage similar to that observed in discrete element modelling; see Section 4. To incorporate the dependence of the viscosity on porosity, the continuous model has to be modified accordingly, as will be discussed in more detail elsewhere.

Before the results obtained are summarized and briefly discussed and conclusions are drawn we note that the developed full-scale finite element model of sintering can be tightly integrated with the results of modelling on various scales. This integration includes, in particular, analysis of diffusion at the atomic scale, calculations of the sintering stress using phase-field and discrete element methods, estimations of the mechanical properties and viscosity by applying a simple model of shrinkage based on experimental correlations, and analysis of initial redistribution of particles using discrete element modelling. The proposed integration is expected to improve the reliability and accuracy of the predicting nonlinear shrinkage providing at the same time insight into the microstructure of sintered samples.

7. Summary and Discussion

The analysis presented describes nonlinear shrinkage using numerical methods that allow estimation of anisotropic dimensional change during sintering in the bound metal deposition process on various physical scales. The multi-scale approach includes (i) molecular dynamics of sintering of particles with diameters of a few tens of nanometers, on a scale of nanoseconds, in Section 2; (ii) phase-field methods of sintering metal particles in 2D and 3D on the scale of tens of microns (in cross-section, or one filament) and a time scale of hours, in Section 3; (iv) discrete element modelling of sintering on the scale of millimetres (sub-models) formed by tens of thousands particles on a time scale of tens of minutes, Section 4; (v) continuous finite element modelling of the whole part on a time scale of several hours, Section 6. In addition, the correlations between structural and mechanical properties of the sintered samples have been analysed, and a simple method for estimation of nonlinear shrinkage has been proposed, based on these correlations, in Section 5. The main results of the enterprise will now be discussed.

Molecular dynamics (Section 2) simulations were developed to estimate important sintering parameters including the width of a grain boundary and the diffusion coefficients. In particular, it was shown that the grain boundary width δ_{gb} can be $\sim 1.0 \mu\text{m}$ for particles of diameter $\sim 30 \mu\text{m}$, while the value of the surface diffusion coefficient D_{surf} was estimated to be in the range $\approx 8 \times 10^{-10} \text{ m}^2/\text{s}$ to $1.6 \times 10^{-9} \text{ m}^2/\text{s}$, in agreement with published data. Despite the fact that, at present, the method can handle only a few particles with diameter $\lesssim 50 \text{ nm}$ it offers estimates of some key sintering parameters such as grain boundary width and diffusion coefficients, which are used in theoretical developments [5,49,50] and in the sintering simulations of the microstructure evolution based on the phase-field method.

Phase-field methods (Section 3) were applied to simulate the microstructure evolution in the cross-section of one filament, using the phase-field model of sintering [15,16,86]. In 2D this approach allowed modelling of the sintering of a few tens of “particles” with

diameters of the order of a few microns, on the time scale of hours. In 3D the number of particles was of the order of ten and the length scale was tens of microns. Some of the key parameters of the phase-field model were estimated using MD simulations including the grain boundary width δ_{gb} and the diffusion coefficient D_{surf} . It was estimated that the values of the sintering stress and sintering time are of the order 1 MPa and a few hours respectively. These results agree with experimental observations and, together with estimates of the spatial mass distribution obtained from the discrete element model, can further be used for finite element modelling of the whole part.

The discrete element model (Section 4) was applied to analyse the initial rearrangement of the particles on the scale of a few millimetres for small subsections of the whole part, taking account of the layout of the filaments. The model was developed in KRATOS Multiphysics [33,34], allowing simulation of the translational and rotational motion of hundreds of thousands of interacting particles using the discrete element method. These simulations showed that gravity is a major source of the strong non-linear shrinkage observed in experiments on the ground. It was shown that, in zero-G, the shrinkage is only weakly dependent on the filament layout. At the same time it was shown that sintering in microgravity may result in agglomeration of particles and increased risk of fault formation, including lack of fusion. These data together with analysis of the earlier experimental results and estimates of the nonuniform spatial distributions of solid matter in the samples were further used to develop a simple model of shrinkage and for simulations of the full-scale continuous model.

The simple model of sintering (Section 5) was developed based on experimentally observed correlations, known mathematical results on packing densities, and analysis of shrinkage within the discrete element model. It was shown that the density of sintered samples is one of the key system parameters and can be correlated to the microstructure and mechanical properties of the samples. Accordingly, the simplified model assumes that, below threshold density ~ 0.5 , the metal powder during debinding behaves as a suspension of particles and demonstrates nonlinear shrinkage in the gravity direction. The lower the initial density the stronger the effect of gravity and hence nonlinearity. Above the threshold density the system behaves as a porous metal and shrinkage is nearly uniform. In microgravity, low initial density leads to agglomeration and a higher probability of faults. Therefore, to reduce the nonlinearity on the ground and improve the quality of the samples in microgravity, the initial density has to be as close as possible to the threshold value. The proposed mitigation strategies are based on the earlier experimental results and include e.g, using two-sized distribution to increase the initial powder density, reducing particle sizes, increasing sintering time, controlling the concentration of carbon and oxygen in the alloy, and controlling the binder system.

A full-scale finite element continuous model (Section 6) of anisotropic shrinkage was developed in COMSOL[®]. Two macroscopic models were developed to describe the sintering process. One is based on the Olevsky approach and the other on thermal diffusion of backbone polymer. Both models demonstrate shrinkage of the initial structure of the whole part as a function of processing parameters. Both models predict nearly uniform shrinkage of the structure for high initial density and free boundary conditions. Anisotropic shrinkage was observed for spatial variation of the model parameters. It was shown that, besides gravity, fixed boundary conditions are an important factor of anisotropic shrinkage. The models can predict anisotropic shrinkage and determine the required compensation for the green part. The models depend on the number of phenomenological and experimental parameters that can be estimated with a developed multi-scale approach including sintering stress, diffusion coefficients, viscosity, etc.

8. Conclusions

The approach developed above facilitates the analysis of shrinkage during bound metal deposition, and does so on length scales ranging from 10^{-9} to 1 m and time scales from 10^{-9} to 10^3 s. It provides deep physical insight into the mechanisms of shrinkage

and the mutual connections between scales. In particular, simulations on the atomic scale provide estimations of the widths of the boundary layers, diffusion coefficients, and surface and grain boundary energies, that are subsequently used in phase-field modelling on a microscale. The latter simulations provide estimates of the free energy and sintering stress that are in turn used in the macroscopic modelling of the sintering of the whole part. The estimates of the free energy can also be related to the forces used in the discrete element modelling of shrinkage. The initial particle redistributions, analysed by discrete element modelling, are further incorporated into finite element modelling of the whole part providing additional insight into the interrelations between the physical scales, cf. [12].

The predictions of shrinkage based on the developed multi-scale approach agree well with experimental data. The physics of nonlinear shrinkage and the corresponding changes in free energy are further clarified using a simple model of shrinkage that relates nonlinearity to the properties of particle distributions. A direction for future research relates to the application of neural networks for additive manufacturing, combining traditional physics-based approaches with numerical methods together with data-driven algorithms and techniques [56]. Within this paradigm, one will combine physics-based multi-scale models (including molecular dynamics, phase-field methods, discrete element modelling, and finite element models) with data-driven approaches.

Author Contributions: Funding acquisition, I.M.H. and T.J.P.; Investigation, D.G.L., V.H., K.R.W. and S.B.; Methodology, D.G.L., V.H., S.B., C.E.R., I.M.H. and T.J.P.; Project administration, C.E.R., I.M.H. and T.J.P.; Resources, K.R.W., C.E.R. and T.J.P.; Software, D.G.L., V.H. and S.B.; Supervision, K.R.W., C.E.R., I.M.H. and P.V.E.M.; Writing—original draft, D.G.L. and V.H.; Writing—review & editing, K.R.W., S.B., I.M.H., T.J.P. and P.V.E.M. All authors have read and agreed to the published version of the manuscript.

Funding: NASA Space Technology Mission Directorate.

Informed Consent Statement: Not applicable.

Acknowledgments: We are grateful to Taku Ozawa, Hiroya Nitta, and Kenta Chaki for providing J-OCTA software, support, and valuable discussion.

Conflicts of Interest: The authors declare no conflict of interest.

References

1. Tamir, D.; Siewert, T.A.; Matsubuchi, K.; Lee, F.; Su, R.; Eagar, T.W. IN-SPACE WELDING Visions & Realities. In Proceedings of the Thirtieth Space Congress Yesterday's Vision Is Tomorrow's Reality, Cocoa Beach, FL, USA, 27–30 April 1993; pp. 1–8.
2. Luchinsky, D.G.; Hafiychuk, H.; Hafiychuk, V.; Wheeler, K.R. Molecular Dynamics of ULTEM 9085 for 3D Manufacturing: Spectra, Thermodynamic Properties, and Shear Viscosity. Technical Memorandum NASA/TM-2018-220213, 1 December 2018. Available online: <https://ntrs.nasa.gov/citations/20190026629> (accessed on 26 April 2022).
3. Luchinsky, D.G.; Hafiychuk, H.; Hafiychuk, V.; Chaki, K.; Nitta, H.; Ozawa, T.; Wheeler, K.R.; Prater, T.J.; McClintock, P.V.E. Welding dynamics in an atomistic model of an amorphous polymer blend with polymer–polymer interface. *J. Polym. Sci.* **2020**, *58*, 2051–2061. [[CrossRef](#)]
4. Gonzalez-Gutierrez, J.; Cano, S.; Schuschnigg, S.; Kukla, C.; Sapkota, J.; Holzer, C. Additive manufacturing of metallic and ceramic components by the material extrusion of highly-filled polymers: A review and future perspectives. *Materials* **2018**, *11*, 840. [[CrossRef](#)]
5. Coble, R.L. Effects of particle-size distribution in initial-stage sintering. *J. Am. Ceram. Soc.* **1973**, *56*, 461–466. [[CrossRef](#)]
6. Cabezas-Villa, J.L.; Lemus-Ruiz, J.; Bouvard, D.; Jiménez, O.; Vergara-Hernández, H.J.; Olmos, L. Sintering study of Ti6Al4V powders with different particle sizes and their mechanical properties. *Int. J. Miner. Metall. Mater.* **2018**, *25*, 1389–1401. [[CrossRef](#)]
7. German, R.M. *Sintering: From Empirical Observations to Scientific Principles*; Elsevier: Waltham, MA, USA, 2014. [[CrossRef](#)]
8. Ehrlich, G.; Hudda, F.G. Atomic view of surface self-diffusion: Tungsten on tungsten. *J. Chem. Phys.* **1966**, *44*, 1039–1049. [[CrossRef](#)]
9. German, R.M. Sintering Trajectories: Description on how density, surface area, and grain size change. *JOM* **2016**, *68*, 878–884. [[CrossRef](#)]
10. Staab, T.; Helm, R.; Diegeler, A. On the role of grain boundaries during sintering. *Preprints* **2021**. [[CrossRef](#)]
11. Gong, H.; Snelling, D.; Kardel, K.; Carrano, A. Comparison of stainless steel 316L parts made by FDM- and SLM-based additive manufacturing processes. *JOM* **2018**, *71*, 880–885. [[CrossRef](#)]

12. Vock, S.; Klöden, B.; Kirchner, A.; Weißgärber, T.; Kieback, B. Powders for powder bed fusion: A review. *Prog. Addit. Manuf.* **2019**, *4*, 383–397. [[CrossRef](#)]
13. Koparde, V.N.; Cummings, P.T. Molecular dynamics simulation of titanium dioxide nanoparticle sintering. *J. Phys. Chem. B* **2005**, *109*, 24280–24287. [[CrossRef](#)]
14. Tonks, M.R.; Aagesen, L.K. The phase field method: Mesoscale simulation aiding material discovery. *Annu. Rev. Mater. Res.* **2019**, *49*, 79–102. [[CrossRef](#)]
15. Biswas, S.; Schwen, D.; Singh, J.; Tomar, V. A study of the evolution of microstructure and consolidation kinetics during sintering using a phase field modeling based approach. *Extrem. Mech. Lett.* **2016**, *7*, 78–89. [[CrossRef](#)]
16. Biswas, S.; Schwen, D.; Tomar, V. Implementation of a phase field model for simulating evolution of two powder particles representing microstructural changes during sintering. *J. Mater. Sci.* **2017**, *53*, 5799–5825. [[CrossRef](#)]
17. Nosewicz, S.; Rojek, J.; Pietrzak, K.; Chmielewski, M. Viscoelastic discrete element model of powder sintering. *Powder Technol.* **2013**, *246*, 157–168. [[CrossRef](#)]
18. Rojek, J.; Nosewicz, S.; Jurczak, K.; Chmielewski, M.; Bochenek, K.; Pietrzak, K. Discrete element simulation of powder compaction in cold uniaxial pressing with low pressure. *Comput. Part. Mech.* **2015**, *3*, 513–524. [[CrossRef](#)]
19. Rojek, J.; Nosewicz, S.; Maździarz, M.; Kowalczyk, P.; Wawrzyk, K.; Lumelskyj, D. Modeling of a sintering process at various scales. *Procedia Eng.* **2017**, *177*, 263–270. [[CrossRef](#)]
20. Wawrzyk, K.; Kowalczyk, P.; Nosewicz, S.; Rojek, J. A constitutive model and numerical simulation of sintering processes at macroscopic level. *AIP Conf. Proc.* **2018**, *1922*, 030011. [[CrossRef](#)]
21. Olevsky, E.A. Theory of sintering: From discrete to continuum. *Mater. Sci. Eng. R Rep.* **1998**, *23*, 41–100. [[CrossRef](#)]
22. Olevsky, E.A.; Tikare, V.; Garino, T. Multi-scale study of sintering: A review. *J. Am. Ceram. Soc.* **2006**, *89*, 1914–1922. [[CrossRef](#)]
23. Alvarado-Contreras, J.A.; Olevsky, E.A.; German, R.M. Modeling of gravity-induced shape distortions during sintering of cylindrical specimens. *Mech. Res. Commun.* **2013**, *50*, 8–11. [[CrossRef](#)]
24. Xie, X.; Bennett, J.; Saha, S.; Lu, Y.; Cao, J.; Liu, W.K.; Gan, Z. Mechanistic data-driven prediction of as-built mechanical properties in metal additive manufacturing. *NPJ Comput. Mater.* **2021**, *7*, 86. [[CrossRef](#)]
25. Tonks, M.R.; Zhang, Y.; Biner, S.; Millett, P.C.; Bai, X. Guidance to design grain boundary mobility experiments with molecular dynamics and phase-field modeling. *Acta Mater.* **2013**, *61*, 1373–1382. [[CrossRef](#)]
26. Nosewicz, S.; Rojek, J.; Wawrzyk, K.; Kowalczyk, P.; Maciejewski, G.; Maździarz, M. Multiscale modeling of pressure-assisted sintering. *Comput. Mater. Sci.* **2019**, *156*, 385–395. [[CrossRef](#)]
27. Tuncer, N.; Bose, A. Solid-state metal additive manufacturing: A review. *JOM* **2020**, *72*, 3090–3111. [[CrossRef](#)]
28. Bustillos, J.; Kim, J.; Moridi, A. Lack of fusion in additive manufacturing: Defect or asset? *arXiv* **2021**, arXiv:2104.07014.
29. German, R.M. *Sintering solutions aboard the International Space Station*; NASA/Johnson Space Center: Houston, TX, USA, 2018.
30. Plimpton, S. Fast parallel algorithms for short-range molecular dynamics. *J. Comput. Phys.* **1995**, *117*, 1–19. [[CrossRef](#)]
31. Sirk, T.W.; Moore, S.; Brown, E.F. Characteristics of thermal conductivity in classical water models. *J. Chem. Phys.* **2013**, *138*, 064505. [[CrossRef](#)]
32. Permann, C.J.; Gaston, D.R.; Andrš, D.; Carlsen, R.W.; Kong, F.; Lindsay, A.D.; Miller, J.M.; Peterson, J.W.; Slaughter, A.E.; Stogner, R.H.; et al. MOOSE: Enabling massively parallel multiphysics simulation. *SoftwareX* **2020**, *11*, 100430. [[CrossRef](#)]
33. Dadvand, P.; Rossi, R.; Oñate, E. An object-oriented environment for developing finite element codes for multi-disciplinary applications. *Arch. Comput. Methods Eng.* **2010**, *17*, 253–297. [[CrossRef](#)]
34. Dadvand, P.; Rossi, R.; Gil, M.; Martorell, X.; Cotela, J.; Juanpere, E.; Idelsohn, S.; Oñate, E. Migration of a generic multi-physics framework to HPC environments. *Comput. Fluids* **2013**, *80*, 301–309. [[CrossRef](#)]
35. COMSOL. *COMSOL Multiphysics Reference Manual*; Version 5.5; COMSOL Inc.: Stockholm, Sweden, 2020. Available online: www.comsol.com (accessed on 26 April 2022).
36. Rahaman, M.N. *Sintering of Ceramics*; Taylor & Francis Inc.: Boca Raton, FL, USA, 2007.
37. Cannon, R.M.; Carter, W.C. Interplay of sintering microstructures, driving forces, and mass transport mechanisms. *J. Am. Ceram. Soc.* **1989**, *72*, 1550–1555. [[CrossRef](#)]
38. Pino-Minoz, D.; Julien, B.; Drapier, S.; Valdivieso, F. Sintering at particle scale: An Eulerian computing framework to deal with strong topological and material discontinuities. *Arch. Comput. Methods Eng.* **2014**, *21*, 141–187. [[CrossRef](#)]
39. Hirel, P. Atomsk: A tool for manipulating and converting atomic data files. *Comput. Phys. Commun.* **2015**, *197*, 212–219. [[CrossRef](#)]
40. Lee, B.J.; Baskes, M.; Kim, H.; Cho, Y.K. Second nearest-neighbor modified embedded atom method potentials for bcc transition metals. *Phys. Rev. B* **2001**, *64*, 184102. [[CrossRef](#)]
41. Baskes, M.I.; Johnson, R.A. Modified embedded atom potentials for HCP metals. *Model. Simul. Mater. Sci. Eng.* **1994**, *2*, 147–163. [[CrossRef](#)]
42. Elkhateeb, M.G.; Shin, Y.C. Molecular dynamics-based cohesive zone representation of Ti6Al4V/TiC composite interface. *Mater. Des.* **2018**, *155*, 161–169. [[CrossRef](#)]
43. Stukowski, A. Visualization and analysis of atomistic simulation data with OVITO—the Open Visualization Tool. *Model. Simul. Mater. Sci. Eng.* **2010**, *18*, 015012. [[CrossRef](#)]
44. Dzyaloshinskii, I.E.; Lifshitz, E.M.; Pitaevskii, L.P. General theory of van der Waals' forces. *Sov. Phys. Uspekhi* **1961**, *4*, 153–176. [[CrossRef](#)]
45. Gottstein, G. *Grain Boundary Migration in Metals*; Taylor & Francis: Boca Raton, FL, USA, 2010.

46. Wiki. Grain Boundary. 2022. Available online: https://en.wikipedia.org/wiki/Grain_boundary (accessed on 26 April 2022).
47. Luchinsky, D.G.; McClintock, P.V.E. Irreversibility of classical fluctuations studied in analogue electrical circuits. *Nature* **1997**, *389*, 463–466. [[CrossRef](#)]
48. Hozé, N.; Holcman, D. Statistical methods for large ensembles of super-resolution stochastic single particle trajectories in cell biology. *Annu. Rev. Stat. Its Appl.* **2017**, *4*, 189–223. [[CrossRef](#)]
49. Wakai, F.; Brakke, K. Mechanics of sintering for coupled grain boundary and surface diffusion. *Acta Mater.* **2011**, *59*, 5379–5387. [[CrossRef](#)]
50. Pouchly, V.; Maca, K. Master sintering curve: A practical approach to its construction. *Sci. Sinter.* **2010**, *42*, 25–32. [[CrossRef](#)]
51. Moelans, N.; Blanpain, B.; Wollants, P. An introduction to phase-field modeling of microstructure evolution. *Calphad* **2008**, *32*, 268–294. [[CrossRef](#)]
52. Allen, S.M.; Cahn, J.W. A microscopic theory for antiphase boundary motion and its application to antiphase domain coarsening. *Acta Metall.* **1979**, *27*, 1085–1095. [[CrossRef](#)]
53. Zhang, X.; Liao, Y. A phase-field model for solid-state selective laser sintering of metallic materials. *Powder Technol.* **2018**, *339*, 677–685. [[CrossRef](#)]
54. Ahmed, K.; Yablinsky, C.A.; Schulte, A.; Allen, T.; El-Azab, A. Phase field modeling of the effect of porosity on grain growth kinetics in polycrystalline ceramics. *Model. Simul. Mater. Sci. Eng.* **2013**, *21*, 065005. [[CrossRef](#)]
55. Yang, Q.; Kirshtein, A.; Ji, Y.; Liu, C.; Shen, J.; Chen, L.Q. A thermodynamically consistent phase-field model for viscous sintering. *J. Am. Ceram. Soc.* **2018**, *102*, 674–685. [[CrossRef](#)]
56. Luchinsky, D.G.; Hafiychuk, V.; Wheeler, K.R.; Prater, T.J. Analysis of Nonlinear Shrinkage for the Bound Metal Deposition Manufacturing using Multi-scale Approach. Technical Memorandum NASA/TM-20210010310, 11 March 2021. Available online: <https://ntrs.nasa.gov/citations/20210010310> (accessed on 26 April 2022).
57. Wang, G.; Zeng, D.c.; Liu, Z.w. Phase field calculation of interface mobility in a ternary alloy. *Trans. Nonferrous Met. Soc. China* **2012**, *22*, 1711–1716. [[CrossRef](#)]
58. Khachaturyan, A.G. *Theory of Structural Transformations in Solids*; Dover Books on Engineering Series; Dover Publications: Mineola, NY, USA, 2008.
59. Greenquist, I.; Tonks, M.R.; Aagesen, L.K.; Zhang, Y. Development of a microstructural grand potential-based sintering model. *Comput. Mater. Sci.* **2020**, *172*, 109288. [[CrossRef](#)]
60. Dai, G.; Niu, J.; Guo, Y.; Sun, Z.; Dan, Z.; Chang, H.; Zhou, L. Microstructure evolution and grain refinement behavior during hot deformation of Fe micro-alloyed Ti-6Al-4V. *J. Mater. Res. Technol.* **2021**, *15*, 1881–1895. [[CrossRef](#)]
61. German, R.M. *Sintering Theory and Practice*; John Wiley & Sons: Hoboken, NJ, USA, 1996.
62. Cardona, C.G.; Tikare, V.; Patterson, B.R.; Olevsky, E. On sintering stress in complex powder compacts. *J. Am. Ceram. Soc.* **2012**, *95*, 2372–2382. [[CrossRef](#)]
63. Luding, S. Introduction to discrete element methods. *Eur. J. Environ. Civ. Eng.* **2008**, *12*, 785–826. [[CrossRef](#)]
64. Yeom, S.B.; Ha, E.S.; Kim, M.S.; Jeong, S.H.; Hwang, S.J.; Choi, D.H. Application of the discrete element method for manufacturing process simulation in the pharmaceutical industry. *Pharmaceutics* **2019**, *11*, 414. [[CrossRef](#)]
65. SALOME. An Open-Source Software for Pre- and Post-Processing. 2020. Available online: <https://docs.salome-platform.org/latest/gui/GEOM/index.html> (accessed on 26 April 2022).
66. German, R.M. Coordination number changes during powder densification. *Powder Technol.* **2014**, *253*, 368–376. [[CrossRef](#)]
67. Gibson, L.J.; Ashby, M.F. *Cellular Solids: Structure and Properties*, 2nd ed.; Cambridge Solid State Science Series; Cambridge University Press: Cambridge, UK, 1997. [[CrossRef](#)]
68. Phuong, D.; Duong, V.; Luan, V.; Anh, N.; Trinh, V. Microstructure and mechanical properties of Ti6Al4V alloy consolidated by different sintering techniques. *Metals* **2019**, *9*, 1033. [[CrossRef](#)]
69. Téllez-Martínez, J.S.; Olmos, L.; Solorio-García, V.M.; Vergara-Hernández, H.J.; Chávez, J.; Arteaga, D. Processing and characterization of bilayer materials by solid state sintering for orthopedic applications. *Metals* **2021**, *11*, 207. [[CrossRef](#)]
70. Baranau, V.; Tallarek, U. Random-close packing limits for monodisperse and polydisperse hard spheres. *Soft Matter* **2014**, *10*, 3826. [[CrossRef](#)]
71. Mueller, S.; Llewellyn, E.W.; Mader, H.M. The rheology of suspensions of solid particles. *Proc. R. Soc. A Math. Phys. Eng. Sci.* **2009**, *466*, 1201–1228. [[CrossRef](#)]
72. Phillis, G.D.J. Viscosity of suspensions of hard and soft spheres. *arXiv* **2004**, arXiv:cond-mat/0403305.
73. Shewan, H.M.; Stokes, J.R. Analytically predicting the viscosity of hard sphere suspensions from the particle size distribution. *J. Non-Newton. Fluid Mech.* **2015**, *222*, 72–81. [[CrossRef](#)]
74. Yu, A.B.; Standish, N. An analytical—Parametric theory of the random packing of particles. *Powder Technol.* **1988**, *55*, 171–186. [[CrossRef](#)]
75. Dias, R.P.; Teixeira, J.A.; Mota, M.G.; Yelshin, A.I. Particulate binary mixtures: Dependence of packing porosity on particle size ratio. *Ind. Eng. Chem. Res.* **2004**, *43*, 7912–7919. [[CrossRef](#)]
76. Tang, Y.; Huang, Z.; Yang, J.; Xie, Y. Enhancing the capillary force of binder-jetting printing Ti6Al4V and mechanical properties under high temperature sintering by mixing fine powder. *Metals* **2020**, *10*, 1354. [[CrossRef](#)]
77. Cao, F.; Chandran, K.R.; Kumar, P. New approach to achieve high strength powder metallurgy Ti-6Al-4V alloy through accelerated sintering at β -transus temperature and hydrogenation-dehydrogenation treatment. *Scr. Mater.* **2017**, *130*, 22–26. [[CrossRef](#)]

78. bin Suleiman Ahmad, M.J.; bin Abdullah, A.N.; Ibrahim, R.B.; Mohamad, M.; Kasim, N.B.A.; Kadir, M.R.B.D.; Muhamad, S.; Itoh, Y.; Hanada, K.; Shimizu, T. Effect of sintering conditions on mechanical properties and microstructure of titanium alloy produced by metal injection moulding (MIM). *Adv. Mater. Res.* **2013**, *686*, 164–169. [[CrossRef](#)]
79. Azmirruddin, M.; Jabir, M.; Johari, N.; Ibrahim, R.; Hamidi, N. The effect of impurities elements on titanium alloy (Ti-6Al-4V) MIM sintered part properties. *AIP Conf. Proc.* **2017**, *1901*, 040007. [[CrossRef](#)]
80. Ait-Mansour, I.; Kretzschmar, N.; Chekurov, S.; Salmi, M.; Rech, J. Design-dependent shrinkage compensation modeling and mechanical property targeting of metal FFF. *Prog. Addit. Manuf.* **2020**, *5*, 51–57. [[CrossRef](#)]
81. Horvath, R.C.J. *Mastering 3D Printing*; Apress: Berkeley, CA, USA, 2020.
82. Skorokhod, V.V. *Rheological Fundamentals of the Theory of Sintering*; Naukova Dumka Kiev: Kyiv, Ukraine, 1972. (In Russian)
83. Riedel, H. A constitutive model for the finite-element simulation of sintering—Distortions and stresses. In *Ceramic Powder Science III*; Amer Ceramic Society: Westerville, OH, USA, 1990; pp. 619–630.
84. Nowacki, W. *Thermoelasticity*; Pergamon Press PWN-Polish Scientific Publishers: Oxford, UK; New York, NY, USA; Warszawa, Poland, 1986.
85. Sherief, H.H.; Hamza, F.A.; Saleh, H.A. The theory of generalized thermoelastic diffusion. *Int. J. Eng. Sci.* **2004**, *42*, 591–608. [[CrossRef](#)]
86. Wang, Y.U. Computer modeling and simulation of solid-state sintering: A phase field approach. *Acta Mater.* **2006**, *54*, 953–961. [[CrossRef](#)]